Monthly Notices of the ROYAL ASTRONOMICAL SOCIETY

MNRAS **458,** 4250–4268 (2016) doi:10.1093/mnras/stw589
Advance Access publication 2016 March 11

Magnetohydrodynamical simulations of a deep tidal disruption in general relativity

Aleksander Sądowski,[1]★† Emilio Tejeda,[2,3] Emanuel Gafton,[3] Stephan Rosswog[3] and David Abarca[4]

[1]*MIT Kavli Institute for Astrophysics and Space Research 77 Massachusetts Ave, Cambridge, MA 02139, USA*
[2]*Instituto de Astronomía, Universidad Nacional Autónoma de México, AP 70-264, Distrito Federal 04510, Mexico*
[3]*Department of Astronomy and Oskar Klein Centre, Stockholm University, AlbaNova, SE-10691 Stockholm, Sweden*
[4]*Nicolaus Copernicus Astronomical Center, Bartycka 18, PL-00-716 Warsaw, Poland*

Accepted 2016 March 8. Received 2016 March 8; in original form 2015 December 15

ABSTRACT

We perform hydro- and magnetohydrodynamical general-relativistic simulations of a tidal disruption of a $0.1\,\mathrm{M}_\odot$ red dwarf approaching a $10^5\,\mathrm{M}_\odot$ non-rotating massive black hole on a close (impact parameter $\beta = 10$) elliptical (eccentricity $e = 0.97$) orbit. We track the debris self-interaction, circularization and the accompanying accretion through the black hole horizon. We find that the relativistic precession leads to the formation of a self-crossing shock. The dissipated kinetic energy heats up the incoming debris and efficiently generates a quasi-spherical outflow. The self-interaction is modulated because of the feedback exerted by the flow on itself. The debris quickly forms a thick, almost marginally bound disc that remains turbulent for many orbital periods. Initially, the accretion through the black hole horizon results from the self-interaction, while in the later stages it is dominated by the debris originally ejected in the shocked region, as it gradually falls back towards the hole. The effective viscosity in the debris disc stems from the original hydrodynamical turbulence, which dominates over the magnetic component. The radiative efficiency is very low because of low energetics of the gas crossing the horizon and large optical depth that results in photon trapping. Although the parameters of the simulated tidal disruption are probably not representative of most observed events, it is possible to extrapolate some of its properties towards more common configurations.

Key words: accretion, accretion discs – black hole physics – relativistic processes – methods: numerical.

1 INTRODUCTION

Occasionally, stars pass by close enough to a massive black hole (BH) so that the hole's tidal forces overcome the star's self-gravity and the latter is disrupted. Depending on the orbital parameters, a substantial fraction of the star can become unbound – for instance, in the case of a parabolic encounter, 50 per cent of the mass is expelled (Rees 1988). The bound debris returns to the BH at rates that, initially, can significantly exceed the Eddington limit, potentially leading to very luminous transient events.

This fact originally motivated the search for the associated observable events. And indeed, a large and increasing number of candidates for tidal disruption events (TDEs) have been detected. Many of them were discovered in optical and UV sky surveys such as *GALEX* and CFHTLS (Gezari et al. 2008, 2009), PTF (Cenko et al. 2012a; Arcavi et al. 2014), Pan-STARSS (Chornock et al. 2014), SDSS (van Welzen et al. 2011), ROTSE (Vinkó et al. 2014), ASASSN (Holoien et al. 2014, 2015), others were detected in soft X-rays (Komossa & Bade 1999; Halpern, Gezari & Komossa 2004; Maksym, Ulmer & Eracleous 2010; Saxton et al. 2012; Maksym, Lin & Irwin 2014; Lin et al. 2015), while a few unusually long bursts believed to originate in TDEs have also been discovered in the hard X-rays or γ-rays (Bloom et al. 2011; Cenko et al. 2012b; Brown et al. 2015) – see Komossa (2015) and Roth et al. (2015), and references therein.

For constant mass per energy, $\mathrm{d}M/\mathrm{d}E = \mathrm{const}$, Kepler's third law dictates that the bound matter has to be delivered towards the BH at a rate of $\dot{M} \propto t^{-5/3}$ (Rees 1988; Phinney 1989), and many TDE light curves could be modelled with this time dependence. This is to some degree surprising, because the standard picture requires the stellar debris to first circularize, before energy can be efficiently extracted. In standard theory, it is also necessary for a

★ E-mail: asadowsk@mit.edu
† Einstein Postdoctoral Fellow.

sufficiently strong magnetic field to build up and provide an effective turbulent viscosity. The interplay of these two processes determines the ultimate accretion rate through the horizon, and it is at least not obvious that accretion from the circularized flow will follow the same time dependence as the mass return rate.

Another puzzle is the apparent radiative inefficiency of TDEs. If half of a solar mass star is accreted on to a BH, say in a parabolic disruption of a solar-type star, and the accretion converts the rest-mass energy into radiation with the standard efficiency of $\sim$10 per cent, one could expect the total emitted energy to be of the order of 10^{53} erg. However, the observed TDEs do not normally exceed 10^{51} erg, and exhibit typical peak luminosities of $\gtrsim 10^{44}\,\mathrm{erg\,s^{-1}}$ in soft X-rays and $\sim 10^{43}\,\mathrm{erg\,s^{-1}}$ in the *R* band (e.g. Roth et al. 2015). There are multiple ways of explaining this discrepancy, but most likely the accretion that follows a tidal disruption is radiatively inefficient and in this way very different from the standard picture of disc accretion which we believe takes place in active galactic nuclei or galactic BH binaries.

An interesting suggestion to solve these puzzles was recently made by Piran et al. (2015), who proposed that the observed radiation comes only from dissipation in shocks that form when the debris returns on a close orbit to the BH, is deflected because of relativistic apsidal precession, and self-intersects the rest of the incoming stream. In such a way, one could explain the time dependence of the observed light curves – the dissipation in shocks is indeed proportional to the debris return rate. However, a significant fraction of the shocked debris is likely to remain in the innermost region, and one still has to explain why it is not accreting in a radiatively efficient way. If, however, the self-crossing takes place relatively far from the BH, then it will result in changing the orbits of the debris into very eccentric ellipses (Piran et al. 2015). If debris ends up under the horizon after falling along such an orbit, it will not extract energy efficiently – since the specific energy of such an elongated orbit is close to zero. However, the relativistic precession in the innermost region may significantly change this picture.

These are not the only puzzles related to the final fate of stars disrupted by supermassive BHs (SMBHs). Analytical models are obviously limited in their applicability and cannot reliably track the non-linear stages of debris evolution, which instead requires numerical simulations. Such calculations, however, are technically very challenging, since after being disrupted the initial star becomes spread out across a huge volume with non-trivial shape which introduces a very large spread in length- and time-scales. Moreover, in the vicinity of the BH general-relativistic effects are important, while for the disc formation and evolution, radiative transfer and possibly magnetic fields should also be included. So far, tidal disruptions have been evolved mostly using the smoothed particle hydrodynamics (SPH) method (Laguna et al. 1993; Kobayashi et al. 2004; Rosswog, Ramírez-Ruiz & Hix 2008b, 2009; Ramirez-Ruiz & Rosswog 2009; Hayasaki, Stone & Loeb 2013, 2015; Bonnerot et al. 2016; Coughlin & Nixon 2015) or hydrodynamical codes with adaptive mesh refinement (Guillochon & Ramirez-Ruiz 2013; Guillochon, Manukian & Ramirez-Ruiz 2014). Both methodologies can deal well with adapting to the mass distribution, but to date none of the existing approaches accounts properly for the relativistic effects close to the BH, which affect both geodesic motion and gas dynamics.

In this work, we follow a hybrid approach. We use an SPH code that accurately accounts for the self-gravity of the star and its debris to calculate the disruption of a red dwarf (0.1 $\mathrm{M}_\odot$) approaching an SMBH (10^5 $\mathrm{M}_\odot$) on a very close (impact parameter, $\beta = 10$), elliptical ($e = 0.97$) orbit. Once the debris starts to return towards the BH, self-gravity is no longer important and we translate the output from the SPH simulation on to a grid-based general-relativistic magnetohydrodynamics (GRMHD) code where we follow the subsequent evolution of the debris on its way towards the BH. A similar approach has been adopted by Shiokawa et al. (2015). We performed two grid-based simulations, one purely hydrodynamical and another one that accounts for the magnetic field evolution from the onset of the grid-based calculation.

The parameters of the simulated close tidal disruption were chosen for numerical tractability, as will be discussed in the following sections. Although they do not reflect in particular any of the observed events, the simulated debris evolution allows us to understand the physics of most relativistic disruptions. Based on these results, as will be discussed in Section 6, it is also possible to draw conclusions regarding other, more common configurations of tidal disruptions. On the other hand, at high BH mass ($M_{\mathrm{BH}} > 10^7\,\mathrm{M}_\odot$) almost every tidal disruption is close in the relativistic sense (pericentre radius is close to the BH horizon, as is in our case where the pericentre radius is at $\sim 7r_{\mathrm{g}}$). Interestingly, the host galaxies of observed TDEs are much heavier than one would predict from the theory (Stone & Metzger 2016) so the simulated event may be in fact a reasonable representation of most of the TDEs we observe (even though it is an outlier by the standards of the expected TDEs).

The paper is organized as follows. We describe the SPH and the GRMHD methods in Sections 2.1 and 2.2, respectively. Section 3 discusses the tidal disruption we consider. Results for the non-magnetized evolution are presented in Section 4, and Section 5 describes the magnetized case. In the discussion (Section 6), we comment on various caveats that have to be taken into account. Finally, in Section 7 we summarize our findings and the conclusions derived from them.

2 NUMERICAL METHODS

2.1 SPH code

The first stage of the tidal disruption process is simulated with an SPH (Gingold & Monaghan 1977; Lucy 1977) code. SPH is fully Lagrangian and conserves mass, momentum, angular momentum and energy by construction. The major advantage in this context is that the particles directly trace the matter flow and no computational effort is wasted on empty regions. Therefore, the spreading of the initially well-localized spherical star into a huge, geometrically complicated shape can be followed with virtually no additional computational burden. For Eulerian methods, even with an adaptive mesh, covering the huge volume while resolving the relevant density structures is severely challenging, albeit possible. See, e.g., Monaghan (2005), Rosswog (2009, 2015a), Springel (2010) and Price (2012) for recent reviews on SPH, and Rosswog (2015b) for recent improvements of the method.

In this project, we use a relativistic extension of the Newtonian SPH code described in detail in Rosswog et al. (2008a). Previous versions of this code have been used for studying the tidal disruption of white dwarf stars by intermediate-mass BHs (Rosswog et al. 2009) and of main-sequence stars by SMBHs (Gafton et al. 2015). The main modification to this code is a new formulation of the evolution equations that allows us to introduce an exact relativistic treatment of the gravitational and hydrodynamical accelerations acting on each SPH particle. See Tejeda, Gafton & Rosswog (in preparation) for further details and validation of this new implementation. For the present project, the gravitational acceleration due to the central BH corresponds to the exact acceleration acting

on a fluid element in Kerr space–time as computed in Kerr–Schild coordinates. The total force exerted on each SPH particle is complemented by an approximate treatment of the fluid's self-gravity computed in a Newtonian fashion using a binary tree as in Benz et al. (1990). Hydrodynamical shocks are captured by means of an artificial viscosity scheme based on time-dependent parameters that ensure that it is applied only where and when needed (Morris & Monaghan 1997; Rosswog et al. 2000); in addition, a switch to suppress dissipation in pure shear flows (Balsara 1995) is applied.

A red dwarf star is to a good approximation convective and therefore well described by a $\Gamma = 5/3$ polytropic equation of state (EOS). We therefore use this EOS for the initial star and throughout the whole hydrodynamic evolution, both in the SPH and the subsequent GRMHD simulation. During the hydrodynamic evolution, parts of the flow may become radiation-dominated and therefore their EOS might in these regions be better described by a Γ closer to 4/3. But nevertheless, for this initial study we stick to an exponent of $\Gamma = 5/3$, and leave more sophisticated approaches to the EOS for future studies.

2.2 GRMHD code

KORAL was developed in recent years (Sądowski et al. 2013, 2014) and is capable of performing global general-relativistic (GR) radiative (R) magnetohydrodynamical (MHD) simulations of gas dynamics in strong gravitational field of compact objects. KORAL uses a shock-capturing Godunov-based scheme and evolves the equations of GRRMHD in a conservative form. The code adopts the Lax–Friedrichs Riemann solver and uses the MINMOD reconstruction with the diffusivity parameter $\theta = 1.5$. Computations are done in the appropriate fixed GR space–time as described by the Kerr metric of the spinning BH. KORAL uses Kerr–Schild coordinates which allow the inner computational grid boundary to be inside the BH horizon. As a result, the inner boundary is causally disconnected from the domain. KORAL can be used with arbitrary coordinates, i.e. the grid points may be arbitrarily concentrated in the region of interest. KORAL is energy-conserving to machine precision. This is very useful for numerical studies of accretion since energy-conserving schemes correctly convert any magnetic or turbulent energy lost at the grid scale into entropy of the gas.

KORAL performs the computations in geometrical units. From now on, we will report length and time in gravitational units, $r_{\rm g} = GM_{\rm BH}/c^2$ (also denoted here sometimes as M) and $t_{\rm g} = GM_{\rm BH}/c^3$, respectively. We adopt the following definition for the Eddington mass accretion rate,

$$\dot{M}_{\rm Edd} = \frac{L_{\rm Edd}}{0.057c^2}, \quad (1)$$

where $L_{\rm Edd}$ is the Eddington luminosity and 0.057 is the radiative efficiency of a thin disc around a non-rotating BH (Novikov & Thorne 1973). According to this definition, a standard thin, radiatively efficient disc accreting at $\dot{M}_{\rm Edd}$ would have a luminosity of $L_{\rm Edd}$. Table 1 gives conversion factors between CGS and geometrical or Eddington units.

Table 1. Unit conversion.

GU	CGS
$r_{\rm g}$	1.477×10^{10} cm
$t_{\rm g}$	0.493 s
Edd.	CGS
$L_{\rm Edd}$	1.25×10^{43} erg s^{-1}
$\dot{M}_{\rm Edd}$	2.48×10^{23} g s^{-1}

3 TIDAL DISRUPTION SETUP

For this work, we have followed the tidal disruption of a red dwarf initially placed along a bound orbit about a non-rotating BH with mass $M_{\rm BH} = 10^5$ M$_\odot$. The red dwarf has a mass of $M_\star = 0.1$ M$_\odot$, an initial radius of $R_\star = 0.15$ R$_\odot$ and is modelled using 2×10^5 SPH particles initially arranged to reproduce the density profile corresponding to the solution of the Lane–Emden equations for a $\Gamma = 5/3$ polytrope. During the simulation, the fluid reaction to dynamical compression and expansion is also modelled using a polytropic EOS with adiabatic exponent $\Gamma = 5/3$. After its initial setup, the star is subject to a relaxation procedure so that the particles find their equilibrium positions and very closely approximate the true hydrostatic equilibrium solution (Rosswog & Price 2007). Subsequently, the star is placed at a distance of $r_0 = 4\,r_{\rm T}$ from the central BH, where $r_{\rm T} = (M_{\rm BH}/M_\star)^{1/3} R_\star \simeq 71\,r_{\rm g}$ is the tidal radius. The star is imparted an initial velocity that places its centre of mass along a bound orbit with eccentricity $e = 0.97$ and impact parameter $\beta \equiv r_{\rm T}/r_{\rm p} = 10$. This value of the impact parameter corresponds to a pericentre distance of $r_{\rm p} \simeq 7\,r_{\rm g}$. The apocentre distance is $r_{\rm a} \simeq 464\,r_{\rm g}$. Such a choice of parameters is convenient for computational reasons – the whole star can be placed inside the domain during the next, grid-based stage (discussed below), and the dynamical evolution of the debris takes place on a relatively short time-scale, allowing us to place the inner edge of the domain inside the BH horizon.

The initial approach of the star towards the BH and the disruption itself are followed with the SPH code (see the left-hand panel in Fig. 1 for representative snapshots). From this figure, it is clear that the star is completely disrupted after the first pericentre passage. After disruption, the whole stellar gas remains energetically bound to the BH. Nevertheless, by the end of the SPH simulation, only the most tightly bound material has started to fall back on to the BH (though none has yet been accreted), and the less bound material is still expanding outwards. This first part of the simulation comprises about 8×10^3 s of coordinate time and finishes when the head of the disruption debris has returned to a distance of less than $100\,r_{\rm g}$ from the BH.

The final distribution of specific energy E and angular momentum h after disruption is shown in Fig. 2. In Fig. 3, we show the mass distribution with respect to pericentre distances, apocentre distances and eccentricities before and after disruption. By the end of the disruption process, all these three quantities are distributed almost symmetrically about their initial values.

3.1 Mapping on to the KORAL grid

In the second phase of this study, we follow the circularization process and the build-up of the accretion disc using the KORAL code which is better suited to deal with this part of the evolution. To this end, the fluid properties at the end of the SPH simulation were interpolated on to the Eulerian grid used in KORAL .

The KORAL coordinates are a modified version of Kerr–Schild coordinates (Sądowski et al. 2015). The grid points are spaced logarithmically in radius, uniformly in azimuth and are concentrated towards the equatorial plane. The adopted resolution was $256 \times 128 \times 96$ cells in radius, polar angle and azimuth, respectively, allowing for reasonable density of cells in the innermost

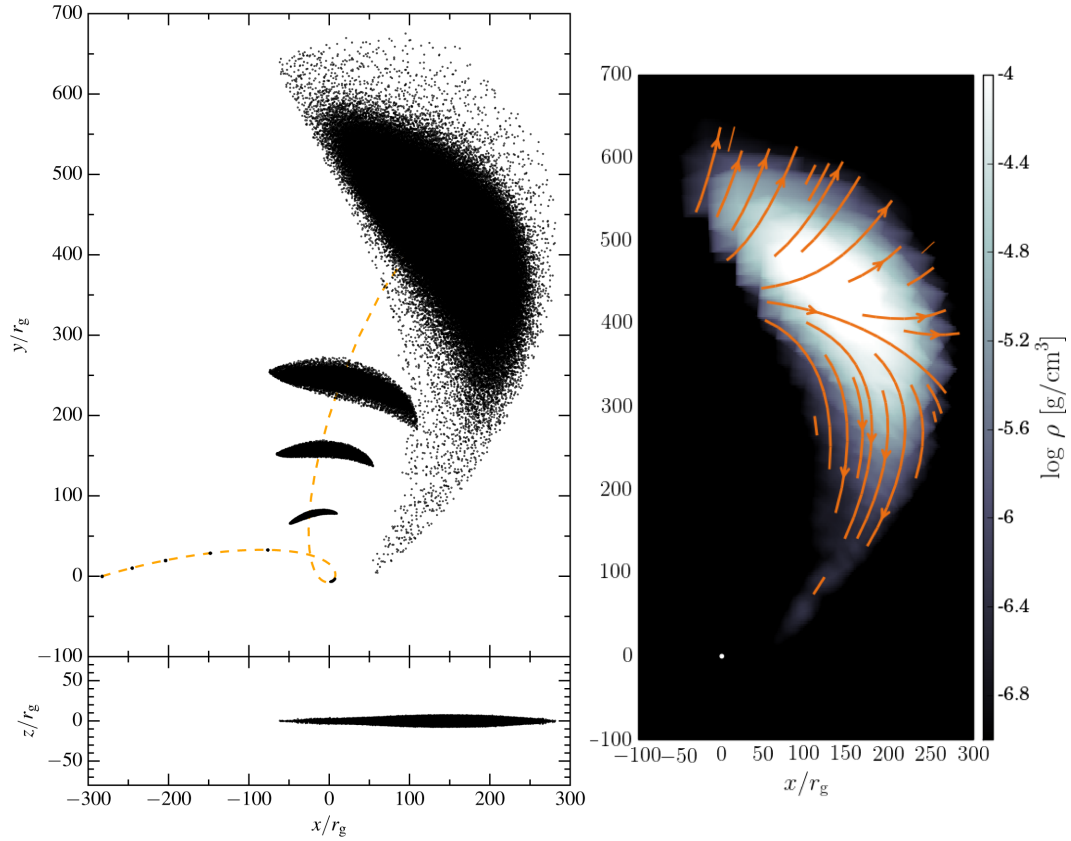

Figure 1. Top left: snapshots of the tidal disruption from the SPH simulation. The last one corresponds to the initial condition of the KORAL simulation. Its projection on the xz plane is shown in the bottom-left panel. Density of points corresponds to the surface density of particles. Right: density on the equatorial plane and gas velocity at the onset of the KORAL simulation, just after translating the SPH output on the grid.

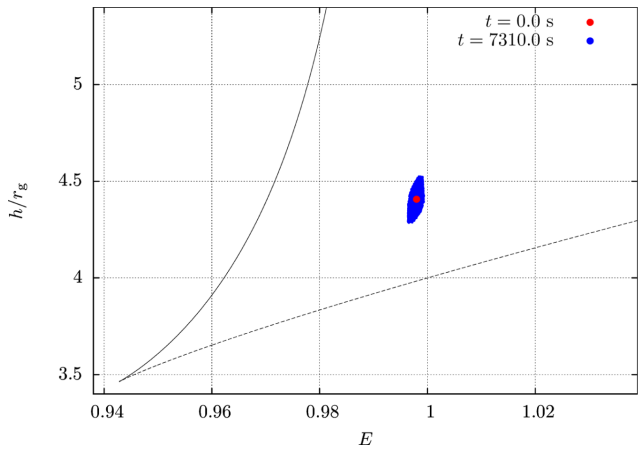

Figure 2. Distribution in relativistic specific energy E and specific angular momentum h after disruption, at the end of the SPH simulation. The red dot indicates the initial values of these quantities at the beginning of the simulation. The domain is delimited by two lines. The upper branch (solid line) corresponds to stable circular motion – geodesic motion can only be found to the right of this line. The lower branch (dashed line) corresponds to unstable circular motion – any point located below this line is in a plunging trajectory towards the BH.

region and near the equatorial plane. The inner radial boundary was placed inside the BH horizon, at $r = 1.85\,r_g$, the outer at $r = 1000\,r_g$. In the polar direction, the grid covered the region within $0.0075\,\text{rad} < \theta < \pi - 0.0075\,\text{rad}$, and we applied the reflective boundary condition at the axis. The angular vertical extent of the cells at the mid-plane was ∼0.01 rad. The grid extended over the full 2π angle in the azimuth.

The output of the SPH simulation was translated on to the KORAL grid by interpolating the relevant quantities (density, temperature and velocities) from the SPH data at the locations corresponding to the centres of the KORAL grid cells. In the end, for consistency, the total amount of gas in the KORAL grid was integrated and normalized in order to recover exactly the mass of the disrupted star ($0.1\,M_\odot$). The grid cells with no corresponding SPH particles were filled with residual atmosphere at rest. With the used SPH particle number we can confidently resolve about five orders of magnitude from the highest to the lowest density. Our atmosphere density in KORAL is typically 10 orders of magnitude lower than the maximum density in the stellar debris and should therefore not introduce any artefacts.

The last snapshot of the SPH simulation shown in the left-hand panel in Fig. 1 reflects the disruption stage when the debris was translated on the KORAL grid. The right-hand panel in the same figure shows the equatorial plane density distribution at that moment, as represented within KORAL . The streamlines reflect the gas velocity. Although the outermost parts of the disrupted star are moving outwards, they are bound and will ultimately fall on to the BH. From that point on, the disruption was evolved within KORAL , with the same polytropic index as in the SPH simulation, $\Gamma = 5/3$, but allowing for non-adiabatic heating.

For the KORAL simulation, we adopted outflow boundary conditions at the inner radial edge located inside the BH horizon and outflow/no inflow boundary conditions at the outer edge. Both the

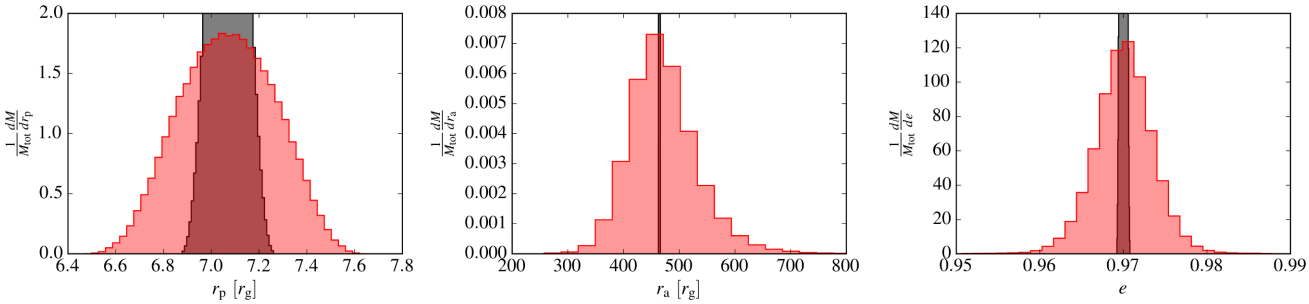

Figure 3. Mass distribution of pericentre distances (left-hand panel), apocentre distances (middle panel) and eccentricities (right-hand panel) before and after disruption (black and red lines, respectively). The two stages shown in each plot also correspond to the first and the last snapshots of the SPH simulation.

non-magnetized and magnetized simulations were run for roughly $130\,000\,t_{\rm g}$, corresponding to approximately 18 h.

4 RESULTS FOR THE NON-MAGNETIZED STAR

We start describing the evolution of the non-magnetized debris. In Section 5, we discuss the changes in this picture when a magnetic field is introduced.

4.1 Self-crossing

Translated on to the KORAL grid, the stellar debris continues its fallback towards the BH. The pericentre of the original stellar orbit was at $r = 7r_{\rm g}$, but the disruption of the star led to a significant spread in orbital energies. The pericentres of the returning debris cover a wider range of radii, with the most bound debris approaching the BH almost directly, at orbits close to plunging ones.

The debris is significantly deflected due to relativistic precession, and does not continue along its original elliptical orbit. Instead, it hits the incoming stream of gas relatively close to the BH. Because of the significant width of the incoming debris stream, resulting mostly from differential velocities imparted during the first pericentre passage of the star on an elliptical orbit (Kochanek 1994; Coughlin et al. 2016), self-crossing takes place at a wide range of radii, $10 \lesssim r/r_{\rm g} \lesssim 100$ (see the top panel in Fig. 4). Effective collision is possible because there is no BH spin-related precession of the orbital plane of the debris.

For the same reason, i.e. relatively compact stellar debris that has experienced strong tidal disruption close to the BH, the nozzle that forms at the pericentres of the orbits of the returning debris is not as thin as it would be for a parabolic encounter. Fig. 5 shows the side view of the spherical slice taken at $r = 10\,r_{\rm g}$, i.e. through the centre of the nozzle. Its vertical extent in the narrowest point is roughly $1\,r_{\rm g}$. At that distance and at the equatorial plane, this width is covered roughly by five polar grid cells. We consider it enough to capture qualitatively the physics taking place there.

Once the gas passes the nozzle, it is relativistically deflected and hits the incoming stream. The middle and bottom panels in Fig. 4 show the gas temperature and entropy, respectively. It is clear that the collision results in a shock – the kinetic energy of the deflected stream is being dissipated and results in rapid increase of temperature and entropy. This 'self-crossing shock' extends along the edge of the incoming stream, from the innermost region out to $r \approx 100\,r_{\rm g}$. The typical velocity of the deflected gas hitting the primary stream from aside is ca. $0.2\,c$. The primary gas has a typical temperature of $10^{8.5}$ K. These parameters result in a Mach number of the order of 20.

In the innermost region, there is a trace of a secondary shock within $r = 20\,r_{\rm g}$ occurring ahead of the self-crossing surface. There is no trace of the 'pancake shock' in the nozzle, which was thick enough not to produce any rapid shock-related heating.

The high gas temperatures are somewhat artificial. Large densities in the inner region result in large optical depths and in establishing local thermal equilibrium between gas and radiation. As in accretion flows accreting at super-Eddington rates, one may expect that it is radiation that provides most of the pressure support. The gas will therefore have, in reality, much lower temperature, with the total pressure of radiation and gas being equal to the gas pressure in the hydrodynamical simulation.

4.2 Outflow

The self-crossing of the stellar debris at small radii results in shock heating. The deflected stream hits the returning tidal stream with a large velocity, of the order of the free-fall velocity at the radius of intersection, $r_{\rm I}$. The magnitude of the specific kinetic energy available for dissipation, $\epsilon_{\rm kin} \approx r_{\rm g}/r_{\rm I} \approx 1/30$ (taking $r_{\rm I} = 30\,r_{\rm g}$ as the representative radius of self-intersection), is much larger not only than the magnitude of the binding energy of the initial stellar orbit, $\epsilon_{\rm bind} = -1/2a \approx 0.002$ (where a is the semi-major axis), but also than the binding energy of the most bound stellar debris, $\epsilon_{\rm bind,\,max} = -1/2a_{\rm min} \approx 0.004$, with $a_{\rm min}$ being the semi-major axis of most bound debris (compare to Fig. 2 which shows the relativistic specific energy, $E = 1 - \epsilon$, of the disrupted star). Therefore, even if only a small fraction of the deflected gas interacts in the shock and only a fraction of its kinetic energy is dissipated, it is likely that the heated gas will get enough thermal energy to become unbound. At the same time, the gas that deposits its kinetic energy into the shock will become more bound. One may also expect that shock-heated gas will expand as a result of the increased thermal pressure.

These two processes are reflected in the panels of Fig. 6, which show vertical slices along $y = 0$ of the gas density (top) and the Bernoulli function (bottom panel) during the self-crossing at an early stage of the simulation. The Bernoulli function was estimated according to (Sądowski & Narayan 2016)

$$\mathrm{Be} = \frac{T^t_t - p + \rho u^t}{\rho u^t}. \tag{2}$$

Positive and negative values of Be correspond to unbound and bound gas, respectively. Streamlines in Fig. 6 reflect the gas velocity projected on the poloidal plane.

The right halves of the panels in Fig. 6 correspond to the cross-section through the stream of the returning stellar debris. It is evident that the gas heated in the shock at the edge of that stream expands and flows out in a quasi-spherical way. The velocity of this outflowing

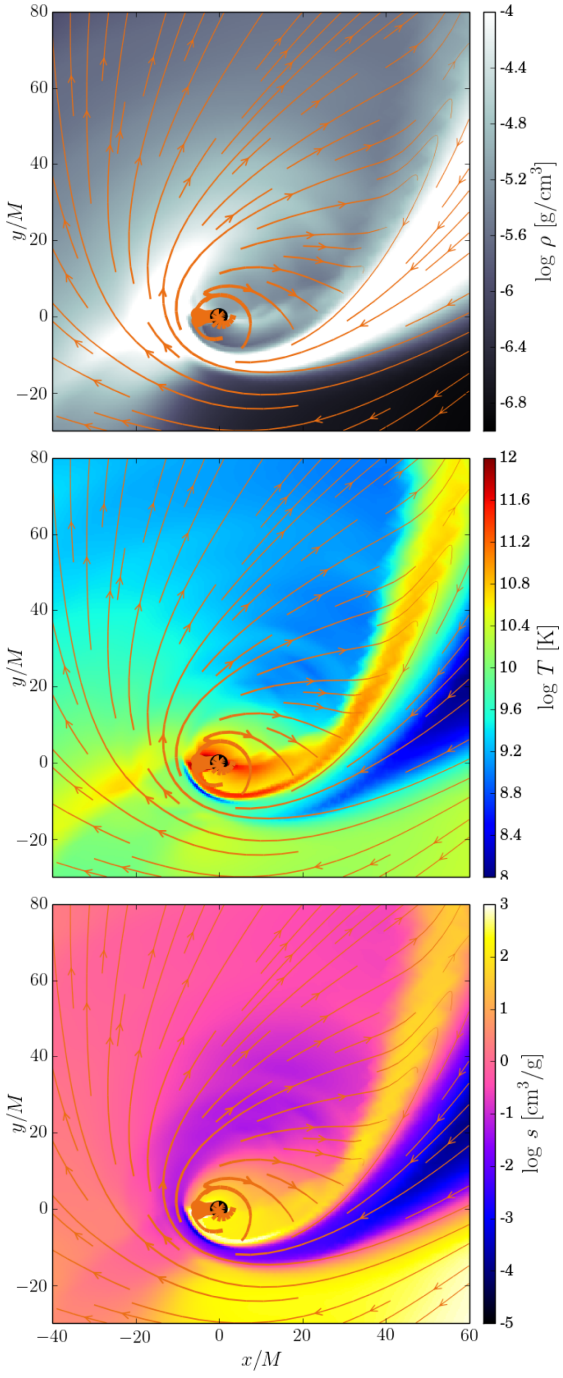

Figure 4. Top to bottom: density, temperature and entropy distributions at $t = 10\,000\,t_g$. Streamlines reflect the gas velocity direction and magnitude.

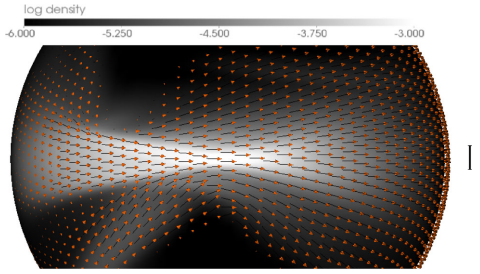

Figure 5. Logarithm of gas density on a spherical slice taken at radius $r = 10\,r_g$. This choice corresponds to the smallest cross-section of the nozzle, visible in the centre. Because of the small pericentre radius and eccentricity of the orbit, the nozzle is relatively thick. The length of the bar on the right corresponds to the vertical extent of 10 grid cells. The arrows reflect the gas velocity.

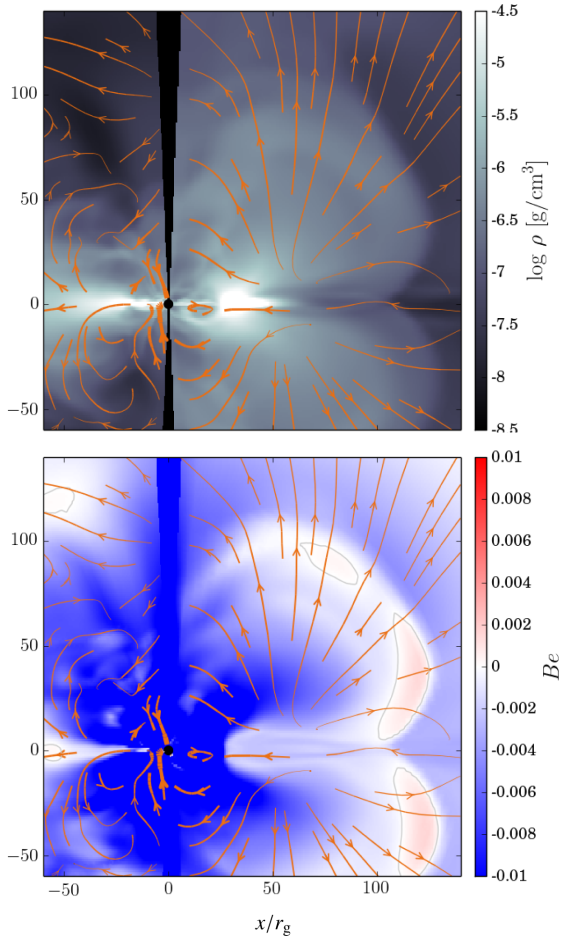

Figure 6. Distribution of gas density (top) and the corresponding Bernoulli function (bottom panel) at the poloidal plane slice taken along $y = 0$. The snapshots correspond to time $t = 10\,000\,t_g$, the same as in Fig. 4. The grey contour in the bottom panel corresponds to Be $= 0$.

gas or the thermal energy contained in it may be large enough to make it unbound. The bottom panel shows the Bernoulli function of gas, with the original binding energy of the debris, ca. -0.003, being rendered in a light blue hue. The outflowing gas is less bound, and some fraction of it can actually become unbound (red hues). This is possible since, simultaneously, the debris that loses its kinetic energy in the shock becomes more bound, as reflected in the deep blue region within $r = 30\,r_g$.

To quantify the amount of gas outflowing due to shock heating in the self-crossing region, we calculated the mass flux crossing spheres of radii $r = 100\,r_g$ and $1000\,r_g$ (the latter being the outer edge of the computational domain). Outflow rates calculated this way are shown in Fig. 7 with grey and red lines, respectively. The outflow through the smaller sphere starts early, at $t \approx 5000\,t_g$, when the first debris that has passed its pericentre reaches a radius $r = 100\,r_g$. Most of this mass flux comes from debris returning to apocentre along its regular orbit in the equatorial plane.

There is also, however, a significant component originating from the quasi-spherical outflow caused by the shock heating of the gas.

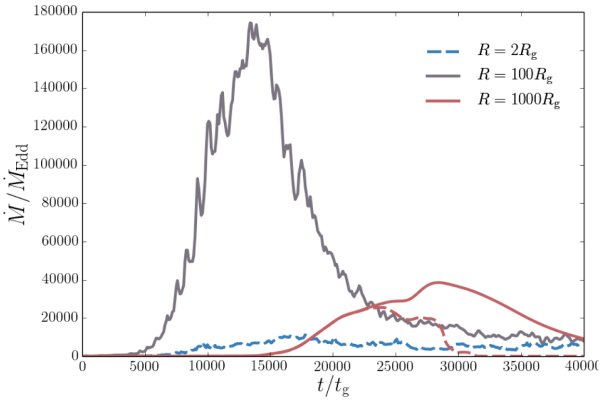

Figure 7. Rate (in Eddington units) at which gas flows out through spheres of given radii. Solid lines reflect the flux of outflowing mass at $r = 100\,r_g$ (grey) and $r = 1000\,r_g$ (red line). The blue dashed line reflects the accretion rate (inward flux) through the BH horizon. The red dashed line shows the flux of unbound gas crossing $r = 1000\,r_g$.

This debris, being less bound than it was initially, can get away from the BH to larger apocentres than those of its original orbits, and parts of it may even leave the computational domain, a fact that would not be possible for the original, completely bound debris. The rate at which gas flows out of the computational domain (at $r = 1000\,r_g$) is denoted by the red line in Fig. 7. The corresponding dashed line reflects the flux of unbound gas crossing the domain boundary.

Gas starts crossing that surface only at $t \approx 15\,000\,t_g$. The lag between the outflow through the outer and inner spheres reflects the typical velocity of the outflow in this region, $v \approx 0.1\,c$. The rate at which the gas flows out through the edge of the computational box is significantly lower, because most of the gas crossing the $r = 100\,r_g$ surface is bound and thus remains close to the BH. However, roughly a third of that gas possesses large enough kinetic energies as to reach $r = 1000\,r_g$ and leave the domain, though only a fraction of that gas, about 40 per cent or $0.015\,M_\odot$, is energetic enough to reach infinity. This means that the bound fraction could in principle fall back on to the volume that is covered by our computational domain. For the time being, we do not account for this effect.

4.3 Periodicity

The rate of gas flowing out through the inner sphere at $r = 100\,r_g$ (denoted by the grey line in Fig. 7) shows a periodic pattern on top of the long-term trend. This feature is clearly visible especially at early times, for $t < 12\,000\,t_g$. The characteristic period is $P \approx 800\,t_g$. The magnitude is not strong enough to overwhelm the general trend reflecting the rate at which mass returns to the BH, but is clearly imprinted in the outflow rate.

This periodicity comes from the feedback of the deflected debris on the original stream. The pericentres of the returning debris' orbits are located very close to the BH, implying significant relativistic precession. As a result, the self-crossing takes place relatively close to the BH (at $10 \lesssim r/r_g \lesssim 100$), with the deflected debris carrying a lot of angular momentum. Consequently, the innermost part of the original stream is not only shock heated, but also gains angular momentum and is therefore pushed at larger radii than its original trajectory. Since a larger pericentre radius is accompanied by less relativistic precession, the subsequent self-crossing episode takes place at larger radii than before, which decreases the efficiency of momentum transfer and allows the incoming stream to revert to (or close to) its original orbit, i.e. to smaller pericentre radii, resulting once again in more effective relativistic precession and angular momentum transfer. The cycle then repeats.

The feedback of the deflected stream on the returning one causes a periodic behaviour with the characteristic time-scale related to the time it takes for the gas to come back to the self-interaction region, i.e. of the order of the Keplerian period at that radius. In the case of our simulation, this period was $t \approx 800\,t_g$, which corresponds to the Keplerian orbital period[1] at $r = 25\,r_g$, located, indeed, within the self-interaction region.

The periodic pattern is clearly imprinted in the outflow rate measured at $r = 100\,r_g$, but is not visible in the rate of gas leaving the computational box (measured at $r = 1000\,r_g$). The reason is that the outflow rate is modulated not only through density but also through velocity. Shells of gas expanding with different velocities quickly overlap each other and cancel out the periodic pattern. If the periodicity were to be detectable in the radiation coming out of the system, photons ought to separate from the gas relatively close to the BH, at $r \lesssim 100\,r_g$. This is not the case in our simulation. As a result of the short duration of the disruption, the gas density is large enough to place the photosphere effectively at the edge of the computational box. The implications of the feedback loop described in this section for more optically thin tidal encounters will be discussed in detail in Section 6.

4.4 Circularization

The self-interaction of the stream dominates the evolution of the system as long as new debris falls into the inner region. Because of the low eccentricity of the considered stellar orbit ($e = 0.97$), all the stellar debris is bound and ultimately returns to the BH, with the least bound stellar debris entering the inner region at about $t = 20\,000\,t_g$. Starting at that time, both the self-crossing and the related ejection of gas cease, while the debris left in the inner region continues to interact; this reduces its average eccentricity and drives it towards circularization.

Fig. 8 shows four snapshots covering the whole duration of the hydrodynamical simulation. The top panels show the distribution of gas density in the equatorial plane, while the bottom panels show the same quantity but on the vertical cross-section along $y = 0$ (as shown with dashed lines in the top panels). The history of the accretion rate at the BH (discussed in Section 4.5) is rendered as a line plot inside the top panels. The snapshots correspond, from left to right, to $t = 5000$, 20 000, 50 000 and 90 000 t_g.

The leftmost panel reflects the early stage of the self-interaction phase, when only the tip of the stellar debris has passed its pericentre. The bottom panel shows only thin structures – the cross-sections through the returning and deflected streams. The next set of panels correspond to the time when the bulk of the debris enters the inner region. Significant amount of gas has already accumulated in the inner region – it is the gas that became strongly bound after its pericentre passage and the subsequent interaction with the incoming stream. The distribution of this gas, however, is very irregular and far from circularized. It resembles the structure seen in the late stages of the simulations performed by Shiokawa et al. (2015), who

[1] The frequency corresponding to the Keplerian period at radius r is in general given by

$$\nu_{\rm Kepl} = 1.022 \times 10^{-3} \left(\frac{10\,r_g}{r}\right)^{3/2} \left(\frac{10^6\,M_\odot}{M_{\rm BH}}\right) \text{ Hz}. \quad (3)$$

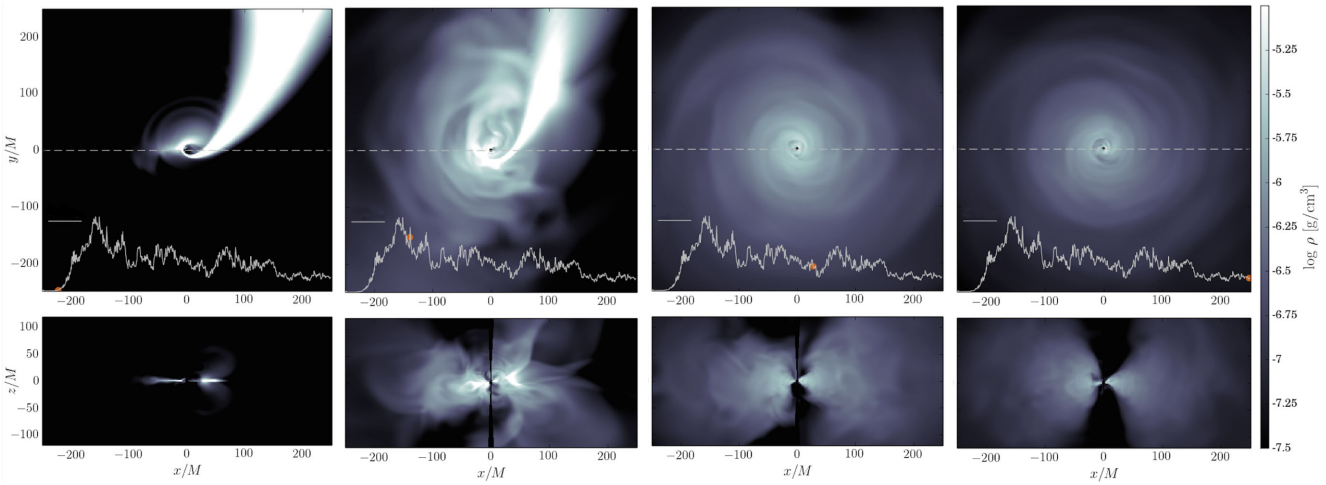

Figure 8. Snapshots of the equatorial plane (top panels) and a slice through the poloidal plane (bottom panels) of the simulated TDE. Colours reflect the logarithm of gas density. The history of the accretion rate through the horizon is shown in the top panels, with the current time of the snapshot being denoted by a red dot. The horizontal lines correspond to $10^4 \dot{M}_{\rm Edd}$. The snapshots were taken at (left to right) $t = 5000\,t_{\rm g}$, $20\,000\,t_{\rm g}$, $50\,000\,t_{\rm g}$ and $89600\,t_{\rm g}$ after the start of the simulation.

simulated a parabolic disruption (with self-crossing occurring at a radius $r \approx 100\,r_{\rm g}$) with debris continuously flowing in.

The last two sets of panels show late stages of the gas evolution. It is evident that, by that time, the gas has circularized and no longer evolves on a dynamical time-scale. The debris has settled down in a very thick disc extending virtually to the edge of the domain. However, most of the debris is located around radius $r = 300\,r_{\rm g}$, i.e. roughly at the distance corresponding to the semi-major axis of the stellar orbit.

4.4.1 Turbulence

Somewhat surprisingly, having in mind that we are dealing so far with a purely hydrodynamical simulation, we see that the debris remains turbulent even long after the circularization. The turbulence is inherited from the initial violent stage of self-interaction and the related feedback loop (Section 4.3), which not only introduces non-axisymmetrical inhomogeneities, but also breaks the equatorial plane asymmetry (in our case originating in the not-perfectly symmetrical SPH initial conditions).

One might expect that once the self-interaction terminates, the turbulence would decay on the eddy turnover time (essentially, the orbital time). However, even after $130\,000\,t_{\rm g}$ from the time when the last debris came into the inner region, i.e. after ca. 55 orbital periods at radius $r = 50\,r_{\rm g}$, the turbulence still persists (although at a slightly lower level than initially, compare the third and fourth panels in Fig. 8).

The question thus arises what process maintains the turbulent properties of the flow. There are two possibilities, either the flow is intrinsically unstable or it is perturbed externally.

Differentially rotating tori in equilibrium are known to be unstable against the Papaloizou & Pringle (1984) instability which requires reflection of acoustic modes at the boundaries. However, the circularized debris extends over a large range of radii, and its inner edge is not well distinguished (see Fig. 12). Moreover, the instability is known to generate $m = 1$ modes (*planets*) which are not present in our simulations. We therefore suspect that the Papaloizou–Pringle instability is not operating.

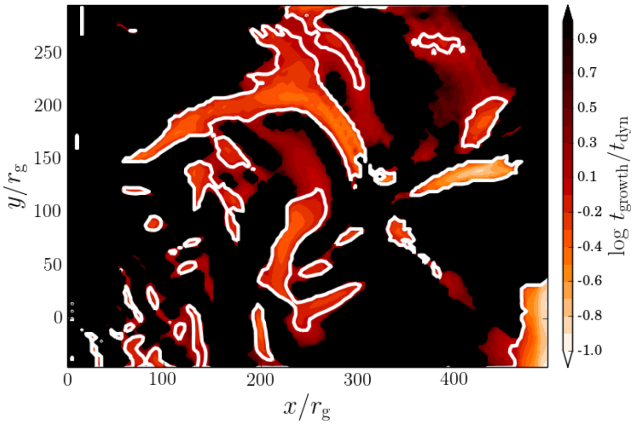

Figure 9. Convective stability of the hydrodynamical simulation calculated using snapshot data taken at $t = 40\,000\,t_{\rm g}$. Black regions denote stable regions. Colours show the logarithm of the growth time-scale over the dynamical time. White contours denote regions where the growth time-scale is shorter than the dynamical time.

Another possibility is convection. We studied the convective stability of the circularized debris following Tassoul (1978). Fig. 9 shows the results of the stability analysis for snapshot data taken at the onset of the circularization phase. Black areas reflect the stable regions, while colours denote unstable ones. The brighter the colour, the shorter the growth time-scale of the convective instability. White contours limit the regions where it is shorter than the dynamical time-scale. The analysis based on the snapshot data shows that some fraction of the volume is indeed unstable against convection and that it is likely to grow because of relatively short growth time-scales. We conclude that the debris is partially unstable against convection and that it may be a crucial factor in keeping the originally disturbed debris turbulent over a long time.

Another possibility is the external perturbation. Indeed, the debris disc is constantly affected by the debris (originally ejected during the self-interaction) falling back in a non-uniform way. It affects the disc by momentum exchange but may also induce a sonic instability (e.g. Glatzel 1988) at the supersonic shear layer that forms at the border of the disc and the polar fallback region.

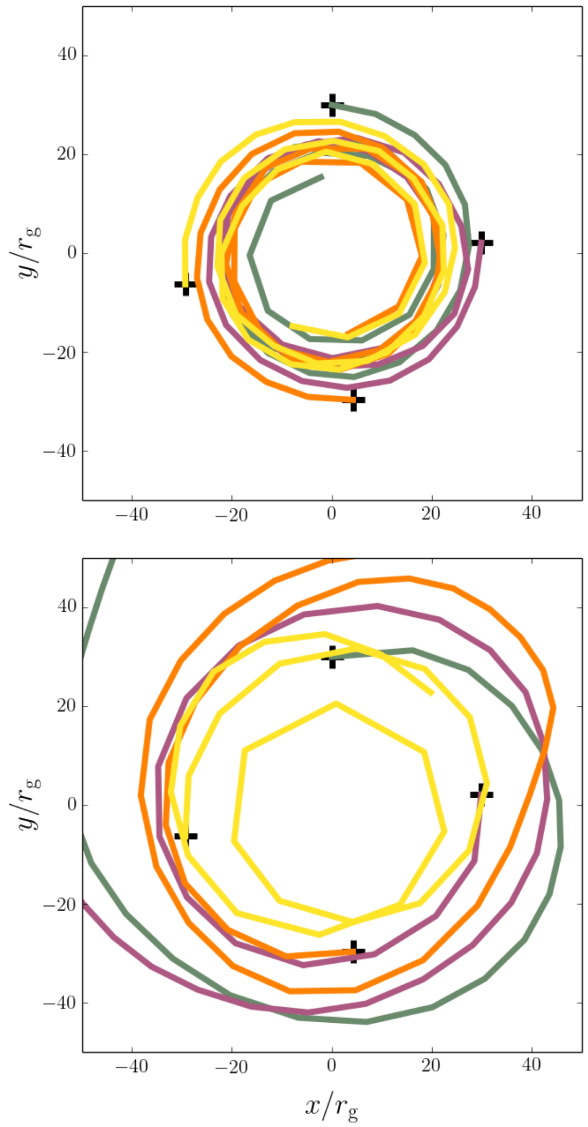

Figure 10. Exemplary trajectories of gas parcels in a standard, supercritical accretion disc (top; Sądowski & Narayan 2016) and in the simulated TDE circularized debris (bottom panel). The trajectories start at the same moment of time ($t = 10\,000\,t_g$ for the supercritical disc and $t = 50\,000\,t_g$ for the TDE debris), in the equatorial plane at the locations denoted by black crosses.

Singling out which factor dominates in sustaining the turbulence, either convection or fallback, would require additional studies which we postpone to the future.

The flow circularizes forming a well-defined toroidal rotating structure, though the gas parcels do not move along perfectly circular orbits, but rather violently move in and out with radial velocities of similar magnitude to the orbital velocity. A visual comparison of the dynamics of the circularized debris and the standard (evolved) accretion disc is given in Fig. 10, which shows trajectories of four gas parcels that at the same moment of time were located at $r = 30\,r_g$. In the case of standard accretion (top panel), gas is only slightly sub-Keplerian and thus follows almost circular trajectories, gradually approaching the BH. In the case of our circularized debris (bottom panel), the dynamics is completely different. The low angular momentum and significant energy of the gas make its trajectories less uniform, with the radial component of velocity often comparable to the azimuthal one.

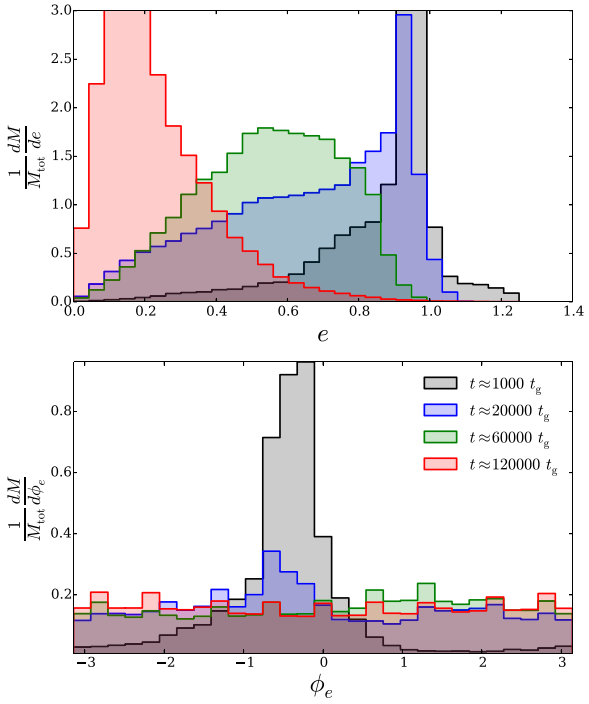

Figure 11. Top: histograms of orbital eccentricity for the gas at radii between $20\,r_g$ and $100\,r_g$. The histograms are normalized so that each bin shows the fractional mass at that eccentricity. Plots are given for four different times where each plot corresponds to a time average spanning approximately $2000\,t_g$ around that time. In physical units, the times correspond to 0.56, 11.27, 33.81 and 67.61 h. Bottom: same as the top, except we are plotting the ϕ component of the eccentricity vector, so that we can track its orientation in the equatorial plane.

Similar behaviour of tidal disruption debris interacting with itself and circularizing to a turbulent thick disc in which gas parcels do not follow circular orbits for a long time was recently observed in SPH simulations of interacting streams (Gafton, private communication).

The azimuthal stress resulting from hydrodynamical turbulence is significant. The corresponding α parameter is ca. 0.1 near $r = 20\,r_g$) (Section 5.3). The viscosity transports the angular momentum outwards and allows the gas deep in the disc to approach the BH. However, as will be discussed in Section 4.5, this process is not the dominant source of the gas crossing the BH horizon.

Finally, we stress that the observed high power in turbulence results from the fact that the self-interaction took place close to the BH, what made it efficient in dissipating and transferring significant amounts of energy.

4.4.2 *Eccentricities*

We will now discuss the circularization process in terms of the eccentricities of the gas orbits throughout the grid-based simulation. At the onset of the simulation, the gas inherited eccentricities and orbit orientations from the SPH simulation (Figs 2 and 3). As a result, the gas approached the BH along these orbits and only after the pericentre passage did the orbital parameters start to change.

Fig. 11 shows how the eccentricities of gas parcels (top panel) and the orientations of their orbits (defined through the azimuth of the eccentricity vector projected on the equatorial plane; bottom panel) evolve with time for gas within $\pi/6$ rad from the equatorial plane. The eccentricities were obtained by taking the local gas velocity vector and the local gradient of pressure, and calculating

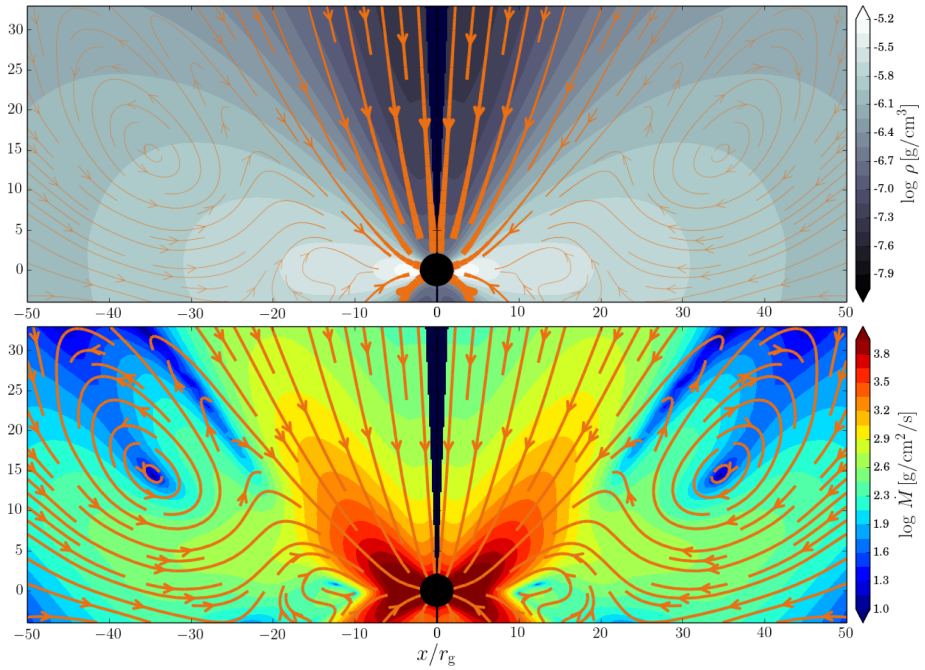

Figure 12. Top panel: time- and azimuth-averaged distribution of density on the poloidal plane corresponding to the debris evolution after the circularization. The streamlines show the poloidal component of gas velocity. Their thickness reflects the velocity magnitude. Bottom panel: local accretion rate in the poloidal plane, $\dot{M} = \rho u^p$, corresponding to the same data. Colours reflect the logarithm of the accretion rate.

the effective velocity vector which produces the same net centrifugal force acting on the gas in the simulation.

The four histograms shown in the panels correspond to a very early stage of the simulation ($t \approx 1000\,t_g$, grey), the end of the self-crossing stage ($t \approx 20\,000\,t_g$, blue) and two phases of quasi-circularization ($t \approx 60\,000\,t_g$, green, and $t \approx 120\,000\,t_g$, red). The early distribution of eccentricities closely resembles the parameters of the stellar orbit, i.e. the eccentricities peaking at $e = 0.97$ and common orientation for the gas orbits. The self-interaction initiates the process of circularization, extending the distribution of eccentricities to much lower values, and broadening the distribution of orbit orientations. Once the self-interaction ends, the gas has already formed the quasi-disc (see Fig. 8), and the initial orientation of the stellar orbit has been forgotten (see the blue and red histograms). The eccentricities, however, do not become zero. As the top panel shows, even at the very end of the simulation, the eccentricities of gas parcels cover a wide range, $0 \lesssim e \lesssim 0.7$. This fact reflects the turbulent nature of the circularized disc – on average the gas moves around the BH, but its motion is far from laminar (Fig. 10).

4.4.3 *Average structure*

The average structure of the inner parts of the disc after the circularization is shown in Fig. 12. The top panel shows the distribution of density in the poloidal plane obtained by averaging in azimuth and in time over $50\,000 < t/t_g < 85\,000$. Colours reflect the density. The disc is indeed very thick, with the average density scaleheight of $h/r \approx 2$, larger than the typical $h/r \approx 0.3$ of standard optically thick accretion discs (e.g. Sądowski et al. 2015).

The streamlines in the same panel reflect the average poloidal components of velocity. The thickness of the lines is roughly proportional to the gas velocity. The fastest inflow occurs in the polar region. Deep inside the disc, the gas hardly moves inwards, with the average, density-weighted velocity of the order of 10^{-3} at $r = 50\,r_g$. Moreover, the velocity pattern is not uniformly pointing inwards, hinting that the averaging period (ca. 20 orbital periods at $r = 40\,r_g$) was not enough to average out the turbulence. Both facts suggest that the accretion through the disc is not efficient.

The bottom panel in Fig. 12 shows the local rate of accretion ($\dot{M} = \rho u^p$) in the poloidal plane. It is evident that the densest interior region of the disc does not contribute significantly to the rate at which gas reaches the BH horizon. This quantity is dominated instead by gas falling down along the edges of the disc. This fallback phenomenon is discussed in the following section.

4.4.4 *Specific energy and angular momentum*

Figs 13 and 14 show the average radial profiles of the specific energy (or Bernoulli function, equation 2) and specific angular momentum. The specific energy of the gas in the circularized disc stays very close to the binding energy of the disrupted star. This means that the remaining gas did not interact strongly enough in the early phases, in contrast to the gas that was involved in the self-crossing shock heating, which either got energetic enough to fly out of the domain, or become bound so much that quickly ended under the BH horizon.

Having at the same time almost marginally bound gas and a circularized disc seems contradictory. Marginally bound gas should follow very eccentric trajectories, not circular orbits, but the situation is complicated by the large thermal pressure that dominates the energy budget. Due to the low angular momentum, the orbital energy of the gas in the disc (dashed red line in Fig. 13) is even lower than the Keplerian value, though the additional contribution of the thermal component (p/ρ) allows the debris to be only weakly bound (solid red line).

The specific angular momentum profile for the circularized debris is shown in Fig. 14. In contrast to a typical disc, the specific angular momentum in the debris is almost constant outside of $r \approx 30\,r_g$

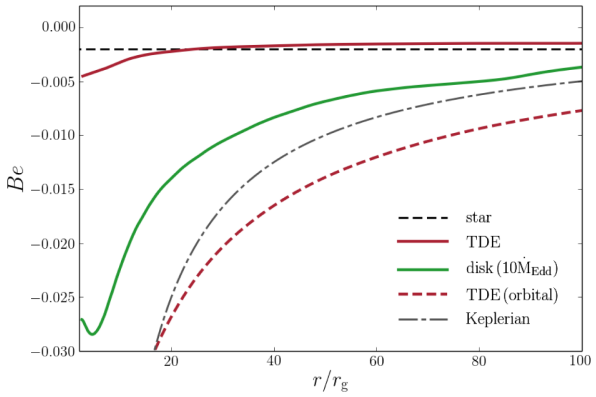

Figure 13. Radial profiles of the average Bernoulli function (specific energy) for the hydrodynamical simulation of a tidal disruption (solid red line) and a typical mildly supercritical accretion disc (solid green line). The dashed red line reflects the orbital energy component of the Bernoulli function of gas in the TDE simulation. For comparison, the specific energy of the star and the Keplerian orbital energy profiles are shown with black dashed and dot–dashed lines, respectively.

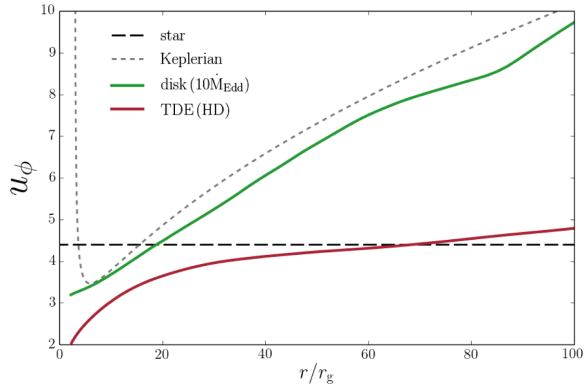

Figure 14. Radial profiles of the average specific angular momentum in the TDE simulation (red line) and a typical geometrically and optically thick accretion disc (green line). The angular momentum of the stellar orbit and the Keplerian profile are also shown.

and very close in value to the angular momentum of the original stellar orbit. This, again, is the region filled with gas that weakly interacted in the early stage of the simulation. At all radii, the angular momentum is sub-Keplerian. Therefore, maintaining equilibrium requires an extra force compensating the missing centrifugal force. In our case, it is the gradient of pressure that supports the disc.

To sum up, the gas relatively quickly circularizes and maintains quasi-stationary, turbulent equilibrium. The disc consists of weakly bound gas with very low angular momentum. High specific energies imply a very large geometrical thickness. In many aspects, the circularized debris resembles the zero-Bernoulli accretion model of Coughlin & Begelman (2014) and agrees with predictions of earlier models of hot accretion flows (e.g. Narayan & Yi 1994; Abramowicz et al. 1995; Blandford & Begelman 1999).

4.5 Direct accretion and fallback

In this section, we look closely into the rate at which gas crosses the BH horizon, i.e. at the BH accretion rate. One can distinguish two phases in the evolution of the tidal debris. Initially, as discussed above, the evolution is strongly affected by the shock heating that develops at the surface where the deflected debris hits the stream

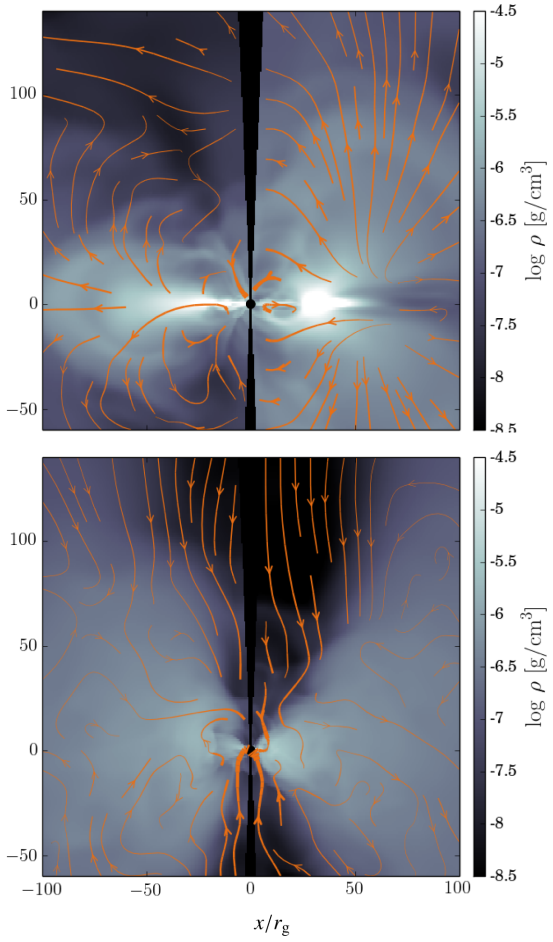

Figure 15. Distribution of density at the slice through the poloidal plane along $y = 0$ at $t = 10\,000\,t_g$ (top) and $t = 80\,000\,t_g$ (bottom panel). The streamlines reflect the velocity field at the same plane.

of returning debris. This process leads to the exchange of energy and momentum between the streams. The returning stream heats up and drives a quasi-spherical outflow. Parts of the deflected stream, however, become more bound and lose angular momentum. As a result, this gas gets closer to the BH and is likely to cross the horizon. This *direct accretion* is the main process driving the BH accretion in the early phase of evolution, while the self-interaction takes place.

As the disc circularizes, rotating gas reaches a state close to equilibrium with the gravitational force balanced by pressure gradient and centrifugal forces. At this stage, direct accretion is no longer possible. To be accreted on to the BH, the gas must now get rid of its angular momentum, though there is no longer a shock surface that could facilitate that. In standard accretion flows, it is viscosity that transports angular momentum outwards. This effect indeed occurs in our simulation, as will be discussed in more detail in Section 5.3, but the accretion driven by viscosity is not the dominant one.

Much stronger accretion takes place close to the axis, along the edges of the rotating disc (see the bottom panel of Fig. 12). Fig. 15 compares the gas dynamics in the poloidal plane at the early, self-crossing stage ($t = 10\,000\,t_g$, top panel) with the properties at the late, after-circularization stage ($t = 80\,000\,t_g$, bottom panel). As long as the self-crossing shock is present, a significant amount of gas is driven out of the equatorial plane, and some fraction of it actually manages to reach the boundaries of and leave the computational domain. The remaining gas is slowed down by gravity and gradually

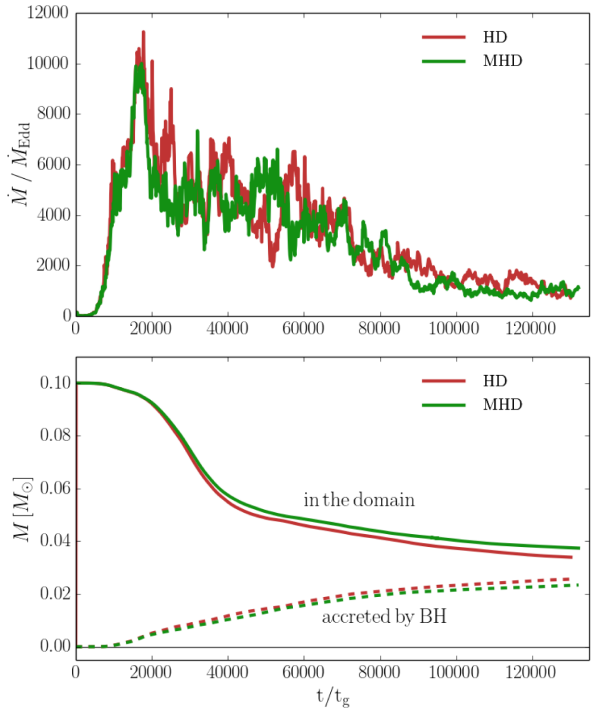

Figure 16. Top panel: history of the accretion rate through the BH horizon for the hydrodynamical (red) and MHD (green line) simulations. Bottom panel: the amount of mass in the computational domain (solid lines) and the mass that has been accreted by given time (dashed lines) for the same simulations.

falls down towards the hole. The portions of gas that were expelled with low angular momentum have a chance to come back almost directly to the BH, ultimately crossing the event horizon, as can be seen from the bottom panel.

The transition between the two mechanisms driving the accretion is smooth. The top panel of Fig. 16 shows the accretion rate history through the BH horizon, calculated as

$$\dot{M} = \int_0^{\pi} \int_0^{2\pi} \sqrt{-g}\, \rho u^r \, \mathrm{d}\varphi \mathrm{d}\theta, \tag{4}$$

where ρ and u^r stand for density and radial component of four-velocity. The peak values are obtained during the self-crossing phase and can reach as much as 10 000 $\dot{M}_{\rm Edd}$. This phase dominates until $t \approx 20\,000\, t_{\rm g}$. At later stages, the fallback of the debris ejected out of the equatorial plane becomes more important, but the transition is not evident. The rate of fallback decreases with time, and one may expect that at some point the viscosity-driven accretion will become dominant. The net accretion rate through the horizon decreases with time and at the end of the simulation reaches ca. 1000 $\dot{M}_{\rm Edd}$ and is still dominated by the fallback, which is, however, stronger than the viscous accretion only by a factor of 2–3 (Section 5.3). Once the fallback becomes unimportant, the debris disc would no longer be perturbed externally and evolve on its own with accretion driven either by convection or magnetorotational instability (MRI), as discussed below.

The bottom panel of Fig. 16 shows the mass contained in the domain (solid lines) and the mass accreted by the BH (dashed lines). In the early stage of the simulation ($10\,000 < t/t_{\rm g} < 20\,000$), the amount of gas in the domain drops faster than the amount of gas accreted by the BH increases. The difference reflects the rate at which the outflowing gas leaves the computational domain. Once the gas circularizes ($t > 20\,000\, t_{\rm g}$), gas ceases to flow out through the outer edge and all the gas lost from the domain ends up inside the BH. By the end of the simulation, 20 per cent of the star (i.e. 0.02 $\mathrm{M}_\odot$) has been accreted by the BH. At the same time, roughly 40 per cent of the stellar gas content stays in the domain, mostly in the circularized disc. The difference, i.e. another 40 per cent, is the amount of gas that has left the computational domain.

5 MAGNETIZED STAR CASE

5.1 Initial setup

In addition to the purely hydrodynamical simulation described above, we performed another one, in which we also evolved the magnetic field. The two simulations used exactly the same initial setup, but for the extra non-zero initial magnetic field inside the stellar debris in the MHD one.

The configuration of the magnetic field in the interior of a star is not well established. Moreover, a tidal disruption introduces additional complexity. If the stellar magnetic field were known, then one should follow its evolution throughout the whole disruption, until the gas falls on to the BH. Recently, an initial effort in this direction has been made by Guillochon (in preparation). However, the SPH code used in our work is not capable of evolving magnetic fields. Neither do we pretend to know how to describe the magnetic field inside a star. Instead, we choose to put a somewhat arbitrary and weak magnetic field inside the stellar debris only at the time when we translate the SPH output on to the KORAL grid. As long as this magnetic field is weak, one can expect that the field that develops in the ultimately circularized debris will not depend on the initial conditions, but will rather be determined by the dynamics of the disc.

We set up the magnetic field at the onset of the grid-based simulation by setting the (only non-zero) azimuthal component of the vector potential to be proportional to gas density, $A^\phi \propto \rho$. The magnetic field is then obtained by calculating the curl of A^i and is thus guaranteed to be divergence-free. The magnitude of the field is then rescaled so that the maximal magnetic-to-gas pressure ratio, β', does not exceed $\beta' = 0.05$. In this way, we obtain a magnetic field that is restricted to the poloidal plane, forming single loops preferentially in the densest regions of the stellar debris.

5.2 Growth of magnetic field

When the stellar debris approaches the BH, it elongates (although, in the case of an elliptical orbit like ours, this effect is limited), compresses and shocks. As a result, the temperature of the debris in the innermost region grows. The magnetic field does not undergo a similar increase. Thus, when the debris that remained in the domain circularizes, the ratio of the magnetic to gas pressures is very low, $\beta' \approx 10^{-7}$, much lower than in the stellar debris at the beginning of the grid-based simulation.

The circularized disc shows significant differential rotation. One can expect that in the presence of non-zero gradient of angular velocity, radial magnetic field lines will be twisted and stretched along the azimuthal direction. The kinetic energy of the rotating flow will be converted into magnetic energy.

The magnetic field in a differentially rotating flow is unstable against the MRI (Balbus & Hawley 1991; Wielgus et al. 2015). When the magnetic field strength is large enough, the induced turbulence starts affecting and dominating the global dynamics and

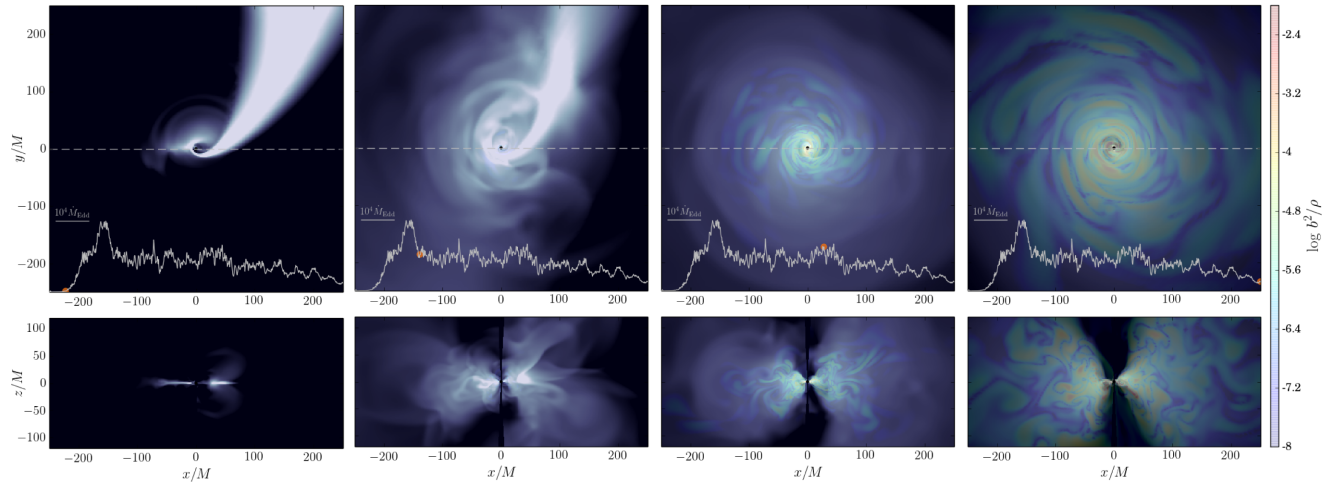

Figure 17. Similar to Fig. 8 but for a magnetized star. Grey colours reflect the gas density while the colours show the magnitude of the, increasing with time, magnetic field.

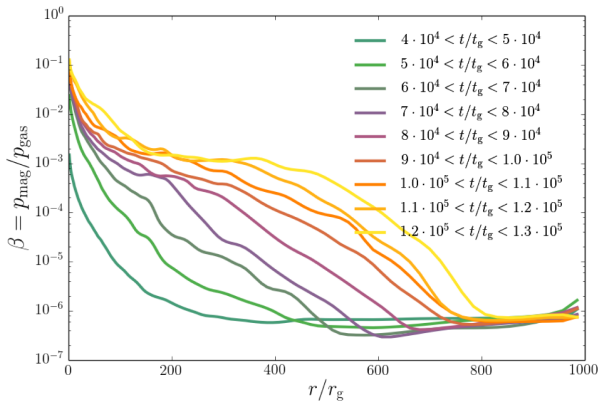

Figure 18. Radial profiles of the magnetic-to-gas pressure ratio, β, in the circularized debris. Lines correspond to the chunks of time specified in the legend with the green and yellow being the earliest and latest, respectively.

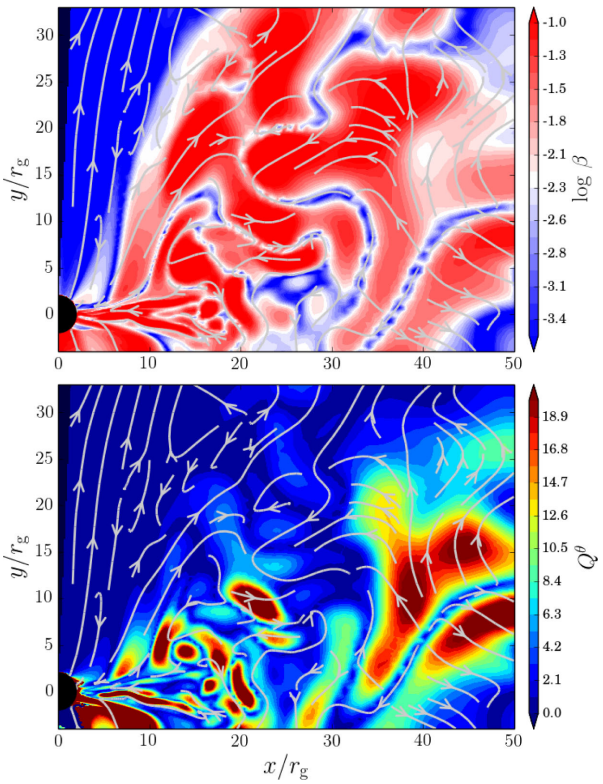

Figure 19. Top panel: magnetic-to-gas pressure ratio at a slice through poloidal place at $t = 120\,000\,t_g$. Bottom panel: the MRI resolution parameter Q^θ (equation 5) plotted in the same way. The arrows reflect the poloidal component of the magnetic field.

leads to the dynamo effect. The saturated state is determined by the rate of shear and non-linear properties of MRI.

The magnetic field must reach some critical strength before the MRI can be resolved in a numerical simulation. The suitable criterion requires that the fastest growing wavelength (which depends on the strength of the magnetic field) must be covered by a reasonable ($\sim$10) number of cells. Therefore, in practice, the magnetic field initially grows only due to the differential rotation, and only at some point the MRI starts to be resolved.

Fig. 17 shows four snapshots of the MHD simulation shown in a similar fashion to Fig. 8. The top and bottom panels reflect the equatorial and poloidal slices, respectively. The density profiles are shown with grey colours, as before. This time, however, the magnetic field strength (here measured as the ratio of magnetic to rest-mass energy densities) is plotted on top of the density profiles with colours. The magnetic field is unimportant for the dynamics in the early phases of the evolution, i.e. during the self-interaction of the debris. Only once the disc circularizes, the magnetic field grows in strength on a dynamical time-scale. It builds up the fastest in the innermost region, where the orbital time is the shortest.

Fig. 18 shows radial profiles of the pressure ratio (magnetic to gas) in the circularized debris obtained by averaging over azimuth and chunks of time lasting $\Delta t = 10\,000\,t_g$. The magnetic field initially grows because of the differential rotation that winds up the magnetic field. The time-scale for this growth increases with the orbital period, and the magnetic field grows fastest in the inner region. Once enough magnetic power has built up to resolve it, the MRI grows exponentially and the magnetic field saturates at the level determined by the non-linear properties of MRI.

Fig. 19 shows the magnetic field properties near the end of the simulation, at $t = 120\,000\,t_g$. The top panel shows the magnetic-to-gas pressure ratio at a slice through the poloidal plane. The magnetic

pressure contributes significantly to the total pressure. In most of the disc interior, its contribution exceeds 10 per cent of the total pressure, a value typical for accretion discs (e.g. Hawley, Gammie & Balbus 1995; Penna et al. 2013). The bottom panel shows the MRI resolution parameter Q^θ defined as (Hawley, Guan & Krolik 2011; Hawley et al. 2013)

$$Q^\theta = \frac{2\pi}{\Omega \Delta x^\theta} \frac{|B^\theta|}{\sqrt{\rho}} \sqrt{g_{\theta\theta}}, \tag{5}$$

where Δx^θ is the grid cell size in θ and Ω is the angular velocity. Wherever the magnetic field is oriented mostly in the polar direction, the MRI resolution parameter reaches its largest values, significantly exceeding $Q^\theta = 10$. The MRI seems to be reasonably well resolved, and one may expect that the magnetically driven turbulence will be present in the simulated flow. However, in contrast to standard accretion flows, it is not dominant here.

5.3 Viscosity

The initial phase of the disruption, i.e. the self-interaction of the streams, is not affected by the magnetic field – which is still relatively weak at that stage. Only once the gas forms the quasi-disc, differential rotation amplifies the field, and magnetic field saturates at the level specific to MRI, may one expect the MHD simulation to differ from the hydrodynamical counterpart. However, this is not the case. As comparison of Figs 8 and 17 suggests, the dynamical properties of the gas do not change. Similarly, the accretion rate through the BH horizon follows the same time dependence (Fig. 16). In this section, we study how important the magnetic field is in sustaining the turbulence and driving the accretion.

The efficiency of a turbulent medium in transporting the angular momentum, and at the same time in driving the gas inwards, can be estimated by calculating the effective turbulent α viscosity parameter. For this purpose, we calculate

$$\alpha = \frac{\langle \widehat{T}^{r\phi} \rangle}{\langle p \rangle}, \tag{6}$$

where $\langle \widehat{T}^{\hat{r}\hat{\phi}} \rangle$ is the average orthonormal r, ϕ component of the stress-energy tensor in the fluid frame and $\langle p \rangle$ is the average gas pressure.

The profiles of the viscosity parameter at different times calculated within $\pi/8$ from the equatorial plane for the MHD simulation are plotted in the top panel of Fig. 20. The solid lines reflect the total stress-energy component, i.e. coming from both the hydro- and magnetohydrodynamical components. The effective α parameter is quite significant and does not evolve significantly with time. It reaches $\alpha \approx 0.4$ at $r = 10\,r_{\rm g}$ and increases even further towards the BH. Such values of the effective viscosity parameter are significantly larger than for regular accretion flows, which exhibit $\alpha \approx 0.1$ at $r = 10\,r_{\rm g}$ (Penna et al. 2013; Sądowski et al. 2015). Does the strong effective viscosity in our simulation come from the magnetic fields?

The total stress-energy tensor can be decomposed into the Reynolds, $T^{r\phi}_{\rm Rey} = (\rho + \Gamma u_{\rm int}) u^r u^\phi$, and Maxwell (magnetic), $T^{r\phi}_{\rm Max} = b^2 u^r u^\phi - b^r b^\phi$, component. The comparison between the two allows us to estimate how important the magnetic field is in transporting the angular momentum. The dashed lines in the top panel of Fig. 20 show the Maxwell component of the viscosity parameter. The magnetic α increased with time, as the magnetic field was building up. It saturated at the level of $\alpha \approx 0.03$ at $r = 10\,r_{\rm g}$, which is roughly an order of magnitude less than the total viscosity parameter. This fact proves that the magnetic fields do not contribute significantly to the angular momentum transfer, which is dominated by the hydrodynamical turbulence left over from the initial violent self-interaction phase and sustained either by convection or by gas constantly falling back on the circularized debris. Similar disproportion of the Maxwell and Reynolds stresses was found in some of the thick accretion flows simulated by McKinney, Tchekhovskoy & Blandford (2012).

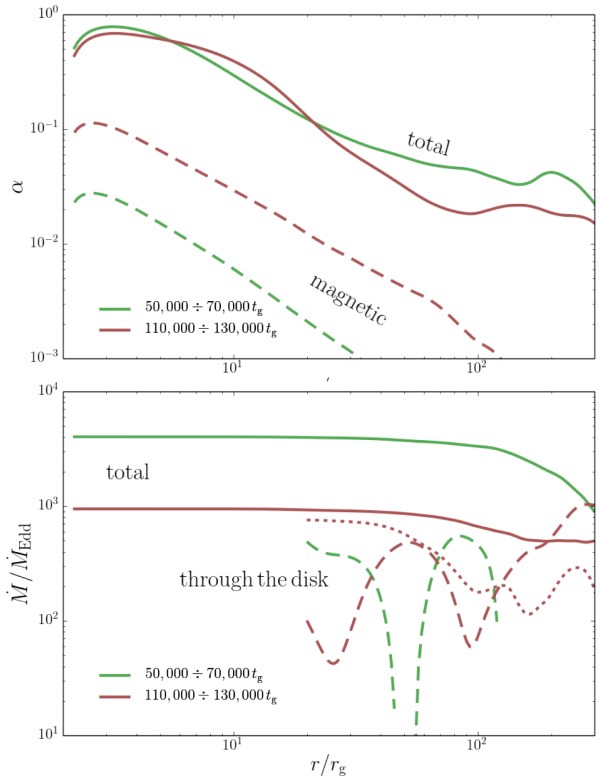

Figure 20. Top panel: the effective viscosity parameter α (equation 6, solid lines) estimated at two stages of the simulation. The dashed lines show the Maxwell component of the former. Bottom panel: radial profiles of the mass accretion rate integrated over the total domain (solid lines) or only inside $\pi/4$ wedge near the equatorial plane (dashed lines). The dotted line shows the estimate of the viscous mass transfer rate based on the α formalism (equation 7).

5.4 Accretion

Because the impact of the magnetic field on the effective viscosity in the quasi-disc is very weak, one may expect that the accretion of gas into the BH will resemble the properties seen before in the hydrodynamical simulation. This is indeed the case. Initially, gas falls on to the BH as a result of self-interaction. This stage is followed by the fallback of gas that has been previously ejected from the innermost region. It turns out that this mode of accretion dominates until the very end of both simulations, and that accretion takes place at similar levels (Fig. 16).

The rate at which the ejected gas falls back on to the BH decreases with time, as less dense gas, ejected to larger distances, returns. As we have shown in the previous section, the gas in the disc is turbulent and the turbulence by itself transfers angular momentum outwards and makes the gas fall towards the BH. The efficiency of turbulent hydrodynamical viscosity does not seem to decrease with time (see the top panel of Fig. 20), so one may expect that at some

point the accretion of gas contained in the disc will overcome the continuously decreasing fallback rate.

We estimate the accretion rate mediated by the turbulence by calculating the mass flux inside the bulk of the disc, outside the innermost region where the flow is strongly affected by the debris falling back, and comparing it with the total accretion rate. The rates are calculated at various radii following equation (4), but limiting the range of polar angles for the former to stay within $\pi/8$ rad from the equatorial plane, which is enough to capture most of the accretion taking place there (compare Fig. 12).

The bottom panel of Fig. 20 shows the radial profiles of the average accretion rate calculated at two stages of the simulation by averaging in time and azimuth. The solid lines reflect the total mass flux. They are flat up to $r \approx 50\,r_{\rm g}$, reflecting the fact that the flow has reached the equilibrium state within this region. However, the rate at which the gas flows on to the BH decreases with time, as a result of the decreasing fallback rate.

Dashed lines in the same plot show the accretion rate inside the bulk of the debris. They are not as flat as the profiles for the whole domain because of two reasons. First, the radial velocities in this region are much lower than the radial velocities of the infalling gas, and it takes longer time to reach equilibrium. Secondly, the gas is not guaranteed to stay inside the region of integration (as it would be required in order to obtain a constant accretion rate profile). Nevertheless, it is possible to approximate the accretion rate driven by turbulent viscosity in the bulk of the debris. It falls between 50 and 500 $\dot{M}_{\rm Edd}$, a range that does not significantly change with time, in agreement with the constancy of the effective viscosity parameter, α, discussed previously.

The turbulence-driven accretion rate may also be estimated using the analytical expression for the radial velocity of an accretion flow (e.g. Frank, King & Raine 1985),

$$u^r \approx \alpha (h/r)^2 \Omega r, \tag{7}$$

where h/r is the scaleheight of the disc and Ω is the angular velocity. The related accretion rate is given through $\dot{M} = 2\pi r \Sigma u^r$, where Σ denotes the surface density. Reading radial profiles of α and Σ from the simulation, estimating $h/r \approx 1$ and calculating the radial velocity using equation (7), we obtain the accretion rate profile plotted with dotted line in the bottom panel of Fig. 20. It has the same order of magnitude as the rate estimated by direct integration of the mass flux inside the debris disc, proving that it is indeed the turbulence that drives the gas towards the BH. However, the rate is lower than the fallback rate even at the end of the simulation, and one would have to wait even longer for the gas driven in this way to dominate the mass flux through the horizon.

6 DISCUSSION

6.1 Optical depth and luminosity

The simulations described in this paper were performed within the framework of GR hydro- and magnetohydrodynamics. The close elliptical disruption that we simulated led to a moderately elongated tidal debris stream returning to the BH after the first pericentre passage. As a result, the optical depths of both the debris and the subsequent circularized disc were very large. The optical depth due to Thompson scattering across the returning debris (Fig. 1) was of the order of 10^7. The circularized debris has the optical depth only an order of magnitude smaller, $\tau \approx$ few $\times\ 10^5$. With such a large amount of gas spread throughout the computational domain, the photosphere is not located within its boundaries. In the initial phase

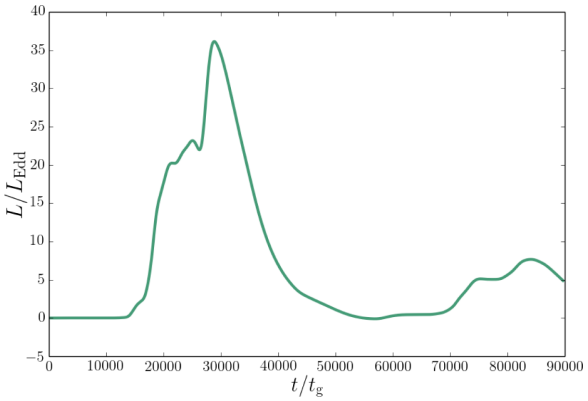

Figure 21. Luminosity (flux of energy integrated over the whole sphere) as a function of time. The luminosity was estimated by taking the advective flux of internal energy crossing the outer edge of computational domain (see equation 8).

of violent self-interaction, the outflow itself is optically thick. In the late, after-circularization stage, the density near the edge of the box is roughly 10^{-10} g cm^{-3}, high enough to provide an optical depth of unity over one gravitational radius, $r_{\rm g} \approx 1.5 \times 10^{10}$ cm.

With the photosphere effectively outside of the computational domain, it made no sense to run an analogous simulation with radiative transfer incorporated (although the KORAL code is capable of that). As long as the gas is very optically thick and the photons do not have an opportunity to detach from the gas, its evolution may be followed with pure hydrodynamics, with an appropriate adiabatic index Γ. We stress here that these conditions would not be satisfied for more realistic and more optically thin events. Similarly, non-zero BH spin and the presence of a magnetic jet could make the most polar region optically thin and allow photons to escape along that route.

However, not resolving the photosphere and evolving the debris as optically thick within the hydrodynamical framework does not allow for direct measurement of the radiative luminosity emerging from the system. To do it properly, one would have to evolve the radiation field in parallel and make sure that the photosphere, where photons decouple from gas, is within the domain. Therefore, we cannot measure the light curve directly.

However, extracting the radiative efficiency would be of interest. The observed TDEs seem to emit less radiation than expected from thin disc accretion of the amount of stellar debris that is bound to the BH, and the reason for this is still unclear (see however, Piran et al. 2015). We can estimate the luminosity extracted from the system by calculating the flux of thermal energy crossing the outer edge of the domain. In radiation pressure-dominated gas, this quantity would approximately correspond to the amount of radiative energy carried by photons advected with the optically thick gas. If no further interaction between gas and radiation takes place outside the boundary, it would also reflect the flux of energy carried away by free-streaming photons or, after integrating over the whole sphere, the total radiative luminosity of the system.

Our estimate of the radiative luminosity is calculated as

$$L = \int_0^{2\pi} \int_0^{\pi} u_{\rm int}\, u^r \sqrt{-g}\, d\theta d\phi, \tag{8}$$

where $u_{\rm int}$ is the internal energy of the gas. Fig. 21 shows the corresponding light curve for the hydrodynamical simulation. The

luminosity increases and reaches maximum when gas flows out through the edge of computational domain, i.e. between 20 000 and 40 000 t_g. This period of time corresponds to the largest flux of thermal energy crossing the boundary and reflects the largest flux of radiative energy carried with optically thick, radiation pressure-supported gas. However, even during this period, the luminosity is only ca. 30 $L_{\rm Edd}$, much less than the outflow accretion rate ($\sim$40 000 $\dot{M}_{\rm Edd}$). Once the outflow ends (which happens when the self-crossing shock is no longer present), the luminosity goes down and hardly any radiation is carried out by the gas. However, our estimate does not include the diffusive flux of radiation, which in principle can be present even in stationary gas. This component, however, will never exceed $L_{\rm Edd}$ in optically thick gas.

Summing up, one can expect a short episode of increased, but moderate, luminosity when gas is ejected during the self-crossing phase. It is followed by a low luminosity despite the fact that the BH is actually accreting at a highly super-Eddington level. The accretion is very inefficient, mostly because gas falling on the BH is almost marginally bound and does not extract significant energy, preventing the production of significantly super-Eddington luminosities.

6.2 The self-crossing feedback loop

In Section 4.3, we have discussed the feedback loop that takes place when the debris returns on a close orbit towards the BH, is deflected due to the apsidal precession and hits the original stream at an angle. The momentum transferred in this way pushes the returning stream outwards, decreasing the efficiency of the feedback exerted by the deflected stream, and allowing the incoming stream to revert to its original trajectory. This feedback modulates the self-crossing and the related dissipation in shocks. It may also results, like in our case, in modulating the rate at which outflows are driven out of the self-intersection region.

This modulation is visible in Fig. 7, where the grey line reflects the rate at which outflowing gas crosses the sphere of radius $r = 100\,r_g$. The red line in the same plot shows the corresponding rate as measured at $r = 1000\,r_g$ (i.e. at the edge of the domain). The periodical imprint is no longer visible, since the modulation of the outflow generation rate results in ejection of consecutive shells moving with different velocities. Such shells collide with each other inside the domain and the initially modulated outflow rate averages out to provide a smooth profile at large radii.

Therefore, although the feedback loop is evident and takes place in the self-intersection region, one should not expect to see the related modulation imprinted on the kinetic energy of the outflow leaving the system, nor on the radiative light curves emerging when the initially optically thick outflow ultimately becomes optically thin.

However, one has to keep in mind that the tidal disruption simulated and analysed in this paper is peculiar because of its ellipticity (although possible sources of highly eccentric TDEs have been discussed by Hayasaki et al. 2013), which prevents the orbit from becoming elongated, leading to the returning debris being extremely optically thick. In the case of a more realistic, parabolic encounter, the debris would consist of gas of lower density and the resulting optical depth would be lower. In such a case, the radiation generated and modulated in the shocked region will decouple from the gas much earlier, and is likely to carry the imprint of the periodicity out to infinity. The characteristic time-scale will roughly correspond to the Keplerian orbital period at the self-intersection radius.

6.3 Extrapolation to parabolic encounters

The star that underwent the tidal disruption described in this work was originally on an eccentric orbit with eccentricity $e = 0.97$. Such a setup was favourable for our simulations – the tidal debris was confined to a relatively small volume and could be translated on to the KORAL grid. Similarly, the time-scale of the disruption and the following debris fallback episode were short, making the computations feasible.

However, such encounters are not very likely. Most stars are directed towards the BH by dynamical interactions with other objects when they are very far from the BH. Thus, they approach the central mass effectively along parabolic orbits.

Parabolic disruptions result in much more elongated streams of returning debris, with half of the stellar mass actually becoming unbound. Therefore, the initial phase of the simulations discussed here, i.e. the self-crossing of the streams, will last longer. In the case discussed in this work, the self-interaction ended when all the debris returned to the BH. In the case of a parabolic disruption, the mass return rate never formally reaches zero, although the amount of mass that falls back will keep decreasing with time. One can expect that the self-intersection – as long as it takes place close to the BH – where plenty of energy is available for dissipation, will dominate the dynamics in the initial phase. However, when the amount of gas that circularized in the inner region is much larger than the gas supply rate at some characteristic time-scale, the incoming stream will no longer be dynamically important to the circularized debris. Thus, as in our case, the self-crossing phase will be followed by circularization.

All the characteristic features of the close, elliptic disruption described in this work will hold for a close, parabolic encounter, although likely with different efficiencies. The self-intersection will result in a feedback loop, which may modulate the emerging light curves. Gas will be ejected from the shocked region and will keep falling back on to the BH for some time. The circularized debris will form a marginally bound quasi-disc, which is likely to provide only moderate or weak turbulent viscosity.

6.4 Extrapolation to lower impact parameters

Many of the properties discussed so far are strictly related to the efficiency of the interaction in the self-crossing shock that forms due to the relativistic precession. The large impact parameter in our simulation translates into a small pericentre radius (in terms of r_g), resulting in significant apsidal precession and in the self-interaction taking place close to the BH. This fact implies that the colliding streams carry significant kinetic energy, which can be dissipated and redistributed between the streams. As a result, a significant fraction of the returning debris gains energy, and an outflow – to some extent unbound – forms. At the same time, a significant amount of debris falls almost directly on the BH. The large amount of energy involved in the violent interaction makes the flow very turbulent, and this turbulence does not decay for many orbital periods, providing – at least initially – the effective viscosity needed for accretion from the debris disc.

One has to be aware, however, that such close encounters as studied in this work are not common. It is unlikely for a star to approach an SMBH along an orbit plunging so deeply into the loss cone. What changes in the described picture if the impact parameter is lower, i.e. if the star does not come as close to the BH? Most importantly, the kinetic energy available for dissipation and redistribution in the self-crossing shock would be lower, leading to

less efficient outflow and less pronounced turbulence. Furthermore, the feedback loop described in Section 4.3 would be less efficient, and the related periodicity would probably disappear. The circularization would proceed along the standard picture, i.e. without any significant outflows preceding it and with little intrinsic turbulence, and the accretion on to the BH would start only after the magnetic field manages to grow and make the debris turbulent. Therefore, the novel features discussed in this work, i.e. the outflow, periodicity and hydrodynamical turbulence, should be regarded as characteristic to close tidal disruptions.

6.5 Impact of BH spin

We have performed simulations of a tidal disruption of a red dwarf by a non-rotating SMBH. A non-zero BH spin would affect two major factors determining the outcome of the debris evolution. First, as long as the star is in the equatorial plane of the BH (the plane perpendicular to the BH spin), a non-zero BH spin would only have a minor contribution to the deflection angle due to the apsidal precession. For BHs rotating against the debris motion (negative BH spin), the self-crossing would take place closer to the BH, most likely resulting in more efficient shocks, leading to larger outflow and direct inflow rates in the initial phase. BH rotation along the debris orbit (positive spin) would move the self-intersection further out, decreasing the efficiency of the shock-related processes, and in particular their associated radiative emission.

However, there is no reason to expect the stellar orbit to lie in the equatorial plane of a spinning BH. If the spin and misalignment angle are large enough, Lense–Thirring precession will change the plane of the debris motion. This will likely result in the deflected stream missing the original one, which will make the shocking less efficient, or not present at all. In such a case, there will be little or no outflow – radiation from the initial, self-crossing phase and the circularization will be delayed. The orbital and spin plane misalignment may therefore explain the disagreement between the observed and predicted rates of TDEs (Stone & Metzger 2016).

6.6 Comparison with other works

Our work combines SPH and grid-based methods to study a close tidal disruption and the following accretion on to the BH. We ran two simulations, with and without magnetic fields. We assumed zero BH spin, an orbital eccentricity of $e = 0.97$ and a mass ratio $M_{\rm BH}/M_* = 10^6$. In recent years, a number of groups performed numerical studies of tidal disruptions and the ensuing circularization. Our work is unique because it consistently evolves magnetic fields and tracks the gas down and across the BH horizon. Below we briefly summarize simulations most similar to ours.

Shiokawa et al. (2015) followed a similar approach, and combined a code allowing the study of a stellar disruption in the tidal gravitational field of a BH (in their case, it was a grid-based code, with the grid comoving with the star, which accounts for self-gravity and applies multipole expansion of the tidal gravitational field) with a grid-based GR hydrodynamical code. The authors studied a disruption of a white dwarf approaching a 500 $M_\odot$ along a parabolic orbit. The inner edge of their simulations was located at $r = 30\,r_{\rm g}$. They found tidal streams self-interacting and identified multiple shocks lasting throughout the simulation. Their results are complementary with ours as they study a different regime – the self-interaction in their case takes place at a much larger distance ($r \approx 1000\,r_{\rm g}$) where less kinetic energy can be dissipated. The existence of multiple shocks in the debris can be explained by the fact that they study a parabolic encounter with a tidal stream of debris constantly flowing into the domain and affecting the already circularized debris.

Bonnerot et al. (2016) studied circularization of the debris using a two-phase SPH approach where the initial disruption is studied including self-gravity, while the following circularization stage is followed without taking it into account. For both stages, they applied the Tejeda & Rosswog (2013) pseudo-Newtonian potential that allows studying the impact of relativistic precession. The authors investigated elliptical orbits ($e = 0.8$) and found that the debris stream circularizes, after a few orbits, at the pericentre radius. They also showed that the structure of the debris disc that forms is sensitive to its cooling efficiency.

All the studies mentioned so far assumed negligible BH spin. As discussed earlier, misaligned orbital and spin planes can lead to inefficient self-interaction. This effect was studied by Hayasaki et al. (2015), who performed SPH simulations with post-Newtonian corrections of multiple elliptical disruptions. They have shown that indeed the Lense–Thirring precession can delay the circularization of the debris.

Similar conclusions were obtained earlier by Haas et al. (2012), who studied a disruption of a white dwarf by an intermediate-mass BH using a grid-based relativistic hydrodynamical code that solves the Einstein equations consistently. The authors also claimed that the luminosity of the debris never exceeds the Eddington luminosity because of photon trapping in the super-Eddington accretion flows.

7 SUMMARY

We have performed two simulations of a close (impact parameter $\beta = 10$), elliptical disruption of a red dwarf star by a non-rotating SMBH. We used an SPH code to simulate the initial passage and subsequent disruption of the star, and a grid-based code to simulate the return of the debris towards the BH. One of the grid simulations was purely hydrodynamical, while the other included a magnetic field seeded at a low level, at the very onset of the grid-based calculations. Our results are summarized as follows.

(i) *Outflow and direct accretion* – Due to the high impact parameter, the simulated debris returns very close to the central BH. The apsidal precession of the orbit results in efficient self-crossing of the streams taking place roughly between $r = 10\,r_{\rm g}$ and $100\,r_{\rm g}$. The deflected stream hits the original one and a shock forms. The kinetic energy of the former is dissipated and the gas is heated up. This interaction redistributes energy and makes the deflected gas more bound, while the shocked gas acquires energy and becomes less bound. As a result, the hot and energetic gas, often unbound, expands and forms a significant quasi-spherical outflow emerging from the self-crossing shock region. In the simulated disruption, roughly 40 per cent of the debris left the computational domain ($1000\,r_{\rm g}$) in this way. The gas that lost energy and became more bound is no longer able to orbit around the BH and crosses the BH horizon.

(ii) *Self-crossing related periodicity* – The deflected stream hits the incoming one and pushes it slightly outwards, increasing its periapsis distance. This, in turn, decreases the apsidal precession angle and moves the self-crossing region further from the BH, decreasing the efficiency of interaction, and allowing the incoming stream to revert to its previous orbit, once again with an increased deflection angle. This phenomenon results in a feedback loop with

characteristic period roughly corresponding to the Keplerian angular momentum at the region of self-intersection (equation 3). The feedback modulates the dissipation taking place in the self-crossing shock. In our simulations, the related periodicity was imprinted on the rate of optically thick outflow generated from the shocked region. However, in more realistic parabolic disruptions, which are more optically thin, the periodicity may be directly visible in the light curves. A necessary condition for the modulation to occur is an efficient self-crossing, which in turn requires a large impact parameter, and either a very small BH spin or an orbital plane perpendicular to the BH spin.

(iii) *Circularized but turbulent marginally bound debris* – The debris forms a rotating thick disc which on average is in equilibrium, but at the same time is turbulent. This turbulence is inherited from the initial violent stage of self-interaction and does not dissipate for a long time. The debris is by itself partially convectively unstable and is constantly perturbed by the gas falling back after being ejected during the shock phase. Both factors help maintain the turbulence. The MRI does not change this picture – the debris remains dominated by the original hydrodynamical turbulence for a long time. It lasts until the end of the simulations we performed, but one may expect that ultimately the MRI-driven turbulence takes over, unless the convection manages to sustain the observed turbulent power.

(iv) *The average properties of circularized debris* – The self-crossing of the tidal stream results in shocks that significantly heat up the gas. However, the total specific energy of the gas in the inner region is close to the specific energy of the stellar orbit (for a parabolic orbit, the corresponding Bernoulli function, Be, would be zero). The high thermal pressure provides a pressure gradient that, together with the centrifugal force, balances out the gravitational force. As a result, the circularized debris is close to marginally bound and follows the general picture of the zero-Bernoulli accretion flow (e.g. Coughlin & Begelman 2014).

(v) *Fallback accretion* – Only a small fraction of the debris that was ejected from the self-crossing shock region is energetically unbound. The bound debris gradually decelerates and after a while starts falling back towards the BH. The original outflow was quasi-spherical. Some fraction of the gas was ejected with low angular momentum, which allows it to fall back almost directly on to the BH. We find that after the initial phase of self-interaction and direct accretion, most of the gas crossing the BH horizon actually comes from the debris falling back in the polar region, along the edges of the disc. Only near the end of the simulations did the fallback rate get close to the estimated turbulence-driven accretion taking place in the debris disc. We predict that fallback accretion dominates for an extended period of time for any close tidal disruption that results in efficient self-crossing near the BH.

(vi) *The effective viscosity* – Surprisingly, we find that magnetic fields do not change significantly the properties of the debris disc. The turbulence inherited from the initial, chaotic and violent self-interaction stage does not decay in either the hydro- or magnetohydrodynamical simulations for many orbital periods. The effective viscosity provided by this turbulence dominates over the viscosity mediated by magnetic fields, and will lead to accretion from the disc once the fallback ceases.

(vii) *Radiative efficiency* – The simulated close tidal disruption is likely to be extremely radiatively inefficient. The initial self-crossing phase led to ejection of optically thick outflow carrying significant kinetic energy. However, the amount of radiation that is likely to reach an observer once that outflow becomes optically thin is not large – despite the outflow rate at the level of $40\,000\,\dot{M}_{\rm Edd}$, the estimated luminosity did not exceed $40\,L_{\rm Edd}$. This picture could change, however, if the kinetic energy of the outflow is dissipated. Neither will the bound debris falling back on to the BH lead to significant radiative emission – such gas is optically thick, hardly bound and falls back in a laminar way. Once the fallback ceases, the accretion from the debris disc will dominate. The radiative efficiency of this process will be lower than for a standard accretion disc because the debris holds to the energy of the original star (so that little energy can be extracted when the gas approaches the horizon). Furthermore, as long as the accretion rate and the optical depth of the debris are large, the efficient photon trapping does not allow for large luminosities.

ACKNOWLEDGEMENTS

The authors thank Nicholas Stone, Ramesh Narayan, Julian Krolik, Chris Fragile, Jean-Pierre Lasota, James Guillochon and Jonatham McKinney for useful comments. AS acknowledges support for this work by NASA through Einstein Postdoctoral Fellowship number PF4-150126 awarded by the Chandra X-ray Center, which is operated by the Smithsonian Astrophysical Observatory for NASA under contract NAS8-03060. AS and EG thank the Harvard-Smithsonian Center for Astrophysics for its hospitality. The work of SR has been supported by the Swedish Research Council (VR) under grant 621-2012-4870. The authors acknowledge computational support from NSF via XSEDE resources (grant TG-AST080026N), from NASA via the High-End Computing (HEC) Program through the NASA Advanced Supercomputing (NAS) Division at Ames Research Center and from the North-German Supercomputing Alliance (HLRN).

REFERENCES

Abramowicz M. A., Chen X., Kato S., Lasota J.-P., Regev O., 1995, ApJ, 438, L37
Arcavi I. et al., 2014, ApJ, 793, 38
Balbus S. A., Hawley J. F., 1991, ApJ, 376, 214
Balsara D. S., 1995, J. Comput. Phys., 121, 357
Benz W., Cameron A. G. W., Press W. H., Bowers R. L., 1990, ApJ, 348, 647
Blandford R. D., Begelman M. C., 1999, MNRAS, 303, L1
Bloom J. et al., 2011, Science, 333, 203
Bonnerot C., Rossi E., Lodato G., Price D. J., 2016, MNRAS, 455, 2253
Brown G. C., Levan A. J., Stanway E. R., Tanvir N. R., Cenko S. B., Berger E., Chornock R., Cucchiaria A., 2015, MNRAS, 452, 4297
Cenko S. B. et al., 2012a, MNRAS, 420, 2684
Cenko S. B. et al., 2012b, ApJ, 753, 77
Chornock R. et al., 2014, ApJ, 780, 44
Coughlin E. R., Begelman M. C., 2014, ApJ, 781, 82
Coughlin E. R., Nixon C., 2015, ApJ, 808, L11
Coughlin E. R., Nixon C., Begelman M. C., Armitage P. J., Price D. J., 2016, MNRAS, 455, 3612
Frank J., King A. R., Raine D. J., 1985, Accretion Power in Astrophysics. Cambridge Univ. Press, Cambridge, p. 283
Gafton E., Tejeda E., Guillochon J., Korobkin O., Rosswog S., 2015, MNRAS, 449, 771
Gezari S. et al., 2008, ApJ, 676, 944
Gezari S. et al., 2009, ApJ, 698, 1367
Gingold R. A., Monaghan J. J., 1977, MNRAS, 181, 375
Glatzel W., 1988, MNRAS, 231, 795
Guillochon J., Ramirez-Ruiz E., 2013, ApJ, 767, 25
Guillochon J., Manukian H., Ramirez-Ruiz E., 2014, ApJ, 783, 23
Haas R., Shcherbakov R. V., Bode T., Laguna P., 2012, ApJ, 749, 117
Halpern J. P., Gezari S., Komossa S., 2004, ApJ, 604, 572

Hawley J. F., Gammie C. F., Balbus S. A., 1995, ApJ, 440, 742
Hawley J. F., Guan X., Krolik J. H., 2011, ApJ, 738, 84
Hawley J. F., Richers S. A., Guan X., Krolik J. H., 2013, ApJ, 772, 102
Hayasaki K., Stone N., Loeb A., 2013, MNRAS, 434, 909
Hayasaki K., Stone N., Loeb A., 2015, preprint (arXiv:1501.05207)
Holoien T. W. S. et al., 2014, MNRAS, 445, 3263
Holoien T. W. S. et al., 2015, MNRAS, 455, 2918
Kobatayshi S., Laguna P., Phinney E. S., Meszaros P., 2004, ApJ, 615, 855
Kochanek C. S., 1994, ApJ, 422, 508
Komossa S., 2015, J. High Energy Astrophys., 7, 147
Komossa S., Bade N., 1999, A&A, 343, 775
Laguna P., Miller W. A., Zurek W. H., Davies M. B., 1993, ApJ, 410, L83
Lin D. et al., 2015, ApJ, 811, 43
Lucy L. B., 1977, AJ, 82, 1013
McKinney J. C., Tchekhovskoy A., Blandford R. D., 2012, MNRAS, 423, 3083
Maksym P., Ulmer M. P., Eracleous M., 2010, ApJ, 722, 1035
Maksym P., Lin D., Irwin J. A., 2014, ApJ, 792, L29
Monaghan J. J., 2005, Rep. Prog. Phys., 68, 1703
Morris J. P., Monaghan J. J., 1997, J. Comput. Phys., 136, 41
Narayan R., Yi I., 1994, ApJ, 428, L13
Novikov I. D., Thorne K. S., 1973, in DeWitt C., DeWitt B., eds, Black Holes. Gordon & Breach, New York
Papaloizou J. C. B., Pringle J. E., 1984, MNRAS, 208, 721
Penna R. F., Sądowski A., Kulkarni A. K., Narayan R., 2013, MNRAS, 428, 2255
Phinney E. S., 1989, in Morris M., ed., Proc. IAU Symp. 136, The Center of the Galaxy. Kluwer, Dordrecht, p. 543
Piran T., Svirski G., Krolik J., Cheng R. M., Shiokawa H., 2015, ApJ, 806, 164
Price D. J., 2012, J. Comput. Phys., 231, 759
Ramirez-Ruiz E., Rosswog S., 2009, ApJ, 679, L77
Rees M. J., 1988, Nature, 333, 523
Rosswog S., 2009, New Astron. Rev., 53, 78
Rosswog S., 2015a, Living Rev. Comput. Astrophys., 1, 1
Rosswog S., 2015b, MNRAS, 448, 3628
Rosswog S., Price D. J., 2007, MNRAS 379, 915
Rosswog S., Davies M. B., Thielemann F.-K., Piran T., 2000, A&A, 360, 171
Rosswog S., Ramírez-Ruiz E., Hix W. R., Dan M., 2008a, Comput. Phys. Commun., 179, 184
Rosswog S., Ramírez-Ruiz E., Hix W. R., 2008b, ApJ, 679, 1385
Rosswog S., Ramírez-Ruiz E., Hix W. R., 2009, ApJ, 695, 404
Roth N., Kasen D., Guillochon J., Ramirez-Ruiz E., 2015, preprint (arXiv:1510.08454)
Saxton R. D., Read A. M., Esquej P., Komossa S., Dougherty S., Rodriguez-Pascual P., Barrado D., 2012, A&A, 541, A106
Shiokawa H., Krolik J. H., Cheng R. M., Piran T., Noble S. C., 2015, ApJ, 804, 85
Springel V., 2010, ARA&A, 48, 391
Stone N. C., Metzger B. D., 2016, MNRAS, 455, 859
Sądowski A., Narayan R., 2016, MNRAS, 456, 3929
Sądowski A., Narayan R., Tchekhovskoy A., Zhu Y., 2013, MNRAS, 429, 3533
Sądowski A., Narayan R., McKinney J. C., Tchekhovskoy A., 2014, MNRAS, 439, 503
Sądowski A., Narayan R., Tchekhovskoy A., Abarca D., Zhu Y., McKinney J. C., 2015, MNRAS, 447, 49
Tassoul J.-L., 1978, Princeton Series in Astrophysics. Princeton Univ. Press, Princeton, NJ
Tejeda E., Rosswog S., 2013, MNRAS, 433, 1930
van Welzen S. et al., 2011, ApJ, 741, 73
Vinkó J. et al., 2014, ApJ, 798, 12
Wielgus M., Fragile P. C., Wang Z., Wilson J., 2015, MNRAS, 447, 3593

This paper has been typeset from a TEX/LATEX file prepared by the author.